Journal Pre-proof

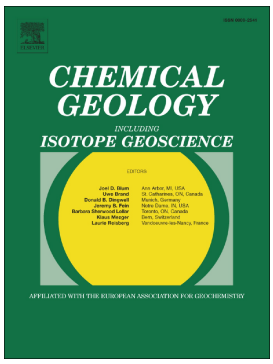

REE+Y uptake and diagenesis in Recent sedimentary apatites

Kaarel Lumiste, Kaarel Mänd, Jake Bailey, Päärn Paiste, Liisa Lang, Aivo Lepland, Kalle Kirsimäe

PII: S0009-2541(19)30360-2

DOI: https://doi.org/10.1016/j.chemgeo.2019.07.034

Reference: CHEMGE 19259

To appear in: *Chemical Geology*

Received date: 8 May 2019

Revised date: 26 July 2019

Accepted date: 28 July 2019

Please cite this article as: K. Lumiste, K. Mänd, J. Bailey, et al., REE+Y uptake and diagenesis in Recent sedimentary apatites, *Chemical Geology* (2018), https://doi.org/10.1016/j.chemgeo.2019.07.034

REE+Y uptake and diagenesis in Recent sedimentary apatites

Kaarel Lumiste[1]*, Kaarel Mänd[1,2], Jake Bailey[3], Päärn Paiste[1], Liisa Lang[1], Aivo Lepland [1,4,5], Kalle Kirsimäe[1]

[1] Department of Geology, University of Tartu, Ravila 14A, 50411 Tartu, Estonia

[2] Department of Earth and Atmospheric Sciences, University of Alberta, Edmonton T6G 2E3, Canada

[3] Department of Earth Sciences, University of Minnesota–Twin Cities, Minneapolis, 55455, USA

[4] CAGE – Centre for Arctic Gas Hydrate, Environment and Climate, Department of Geosciences, UiT The Arctic University of Norway, 9037 Tromsø, Norway

[5] Geological Survey of Norway, 7491 Trondheim, Norway

*Corresponding author: email kaarel.lumiste@ut.ee

Abstract

Rare earth elements and yttrium (REE+Y) distribution in authigenic phases are frequently used as proxies for reconstructing past seawater conditions. Sedimentary apatite precipitates near the sediment-water interface and is therefore capable of recording the REE+Y composition of the overlying water column. While the overprinting of primary REE+Y signal during late stage diagenesis is a widely known phenomenon, less is known about early diagenetic effects. In this study, we investigate the REE+Y distribution in Recent sedimentary apatites found on the Namibian shelf using *in situ* mapping by laser ablation inductively coupled plasma mass spectrometry (LA-ICP-MS). The Namibian phosphorite deposits consist of reworked and redeposited pelletal apatitic grains, ranging from Miocene to Pleistocene in age, and pristine concretionary apatitic grains that formed during Pleistocene to Recent. The results of this study show that the REE+Y signatures of pelletal and concretionary apatitic grains are different with both types showing intragranular variability and differences between grain centers and rims. The REE+Y are concentrated in the external part of the apatitic grains, forming a 10-20 µm wide "enrichment zone". While the central parts of apatitic grains are low in REE+Y (∑REE+Y <450 mg/kg), the external layers can reach ∑REE+Y concentrations as high as 4100 mg/kg. REE+Y

patterns from the center of Recent concretionary apatitic grains are similar to the REE+Y distribution of modern seawater. Enriched rims of Recent concretionary apatitic grains as well as pelletal grains have lost the characteristic modern seawater features: negative Ce-anomaly and high Y/Ho ratio. The REE+Y patterns of these enrichment zones indicate REE+Y scavenging from suboxic-sulfidic pore water after burial or during precipitation at the fluctuating redoxcline. It is evident that REE+Y patterns in bulk digests of authigenic apatite cannot be relied on to record paleoseawater characteristics. Micro-scale REE+Y analyses of apatitic grains can, however, reveal aspects of their diagenetic histories.

Keywords: Rare Earth Elements; REE+Y; sedimentary apatite; early diagenesis; diagenetic overprinting; Namibian phosphorites

1. Introduction

Rare Earth Elements (REE) and Yttrium (together referred to as REE+Y) are a group of elements with remarkably similar chemical and physical properties, yet they are widely used in geochemical studies due to their specific partitioning and fractionation in a wide range of geological processes (Bau, 1996).

While most of the REE+Y typically occur in a trivalent state in geological environments, Ce and Eu show variable valences (Bau et al., 2010). Eu occurs as Eu^{3+} under normal surface conditions and its behavior is analogous to other trivalent REEs, but it is reduced to mobile Eu^{2+} under extremely reducing and/or high temperature (>200 °C) conditions (Bau et al., 2010). In contrast, Ce^{3+} is oxidized to Ce^{4+} in low-temperature oxic conditions (McArthur and Walsh, 1984). The tetravalent Ce is preferentially immobilized in seawater by Fe-Mn oxyhydroxides; hence, in oxygenated and circulated modern oceans, Ce has an anomalously low concentration compared to other REEs (Bau and Koschinsky, 2009)

Similarly, the geochemical twins Y and Ho are decoupled in oxygenated seawater (Bau and Dulski, 1994), resulting in higher Y/Ho ratios in seawater compared to igneous rocks (Minami et al., 1998). Differences in complexation, adsorption and substitution of REEs due to lanthanide contraction (Chen et al., 2015) cause the more stable heavy REEs (HREE; Ho to Lu) to remain in the water column, while light REEs (LREE; La to Nd) are preferably scavenged by sediment particles (Bright et al., 2009). Combined effects of these processes result in modern seawater

REE+Y PAAS (Post Archean Average Shale; Taylor and McLennan, 1985) normalized pattern displaying a negative Ce anomaly, positive Y anomaly (Bau et al., 2010) and HREE enrichment (Shields and Webb, 2004).

Seawater REE+Y characteristics can potentially be captured and preserved in the geological record by authigenic minerals precipitating in equilibrium with seawater (Shields and Stille, 2001). Carbonate and phosphate sediments can record the seawater signature by REE+Y substitution at the Ca site in calcite and apatite crystal structures (Reynard et al., 1999; Elzinga et al., 2002). Amongst the different REE+Y characteristics, Ce anomalies preserved in authigenic phases have been used to study secular changes in seawater redox state (e.g., Lécuyer et al., 2004; Bau and Alexander, 2006; Emsbo et al., 2015; Tostevin et al., 2016; Wallace et al., 2017). However, diagenetic changes in pore water composition (Elderfield and Sholkovitz, 1987) as well as recrystallization of primary minerals (e.g., aragonite and high-Mg calcite recrystallization into low Mg-calcite, or hydroxyapatite alteration into carbonate fluorapatite) can cause modification of primary REE+Y patterns, hence limit their usefulness as proxies for palaeoenvironmental conditions (Azmy et al., 2011; Trueman, 2013; Hood et al., 2018).

Carbonate minerals have been repeatedly shown to retain, despite diagenetic recrystallization (incl. dolomitization), their primary seawater REE+Y pattern (e.g., Bau and Alexander, 2006; Webb et al., 2009; Voigt et al., 2017; Li et al., 2019). Similarly, the REE+Y composition of authigenic sedimentary apatite mainly composed of carbonate fluorapatite (Knudsen and Gunter, 2002) – a thermodynamically stable apatite phase in seawater (Jahnke, 1984) – has been shown to reflect the ambient water conditions for modern (Piper and Bau, 2013) and ancient phosphorites (Shields and Stille, 2001; Emsbo et al., 2015). The thermodynamically unstable bioapatite composed of hydroxyapatite, however, is readily recrystallized and has been shown to be a highly ambiguous carrier of information regarding primary redox conditions (Herwartz et al., 2013; Zhao et al., 2013; Chen et al., 2015; Trotter et al. 2016).

REE+Y uptake and distribution in sedimentary apatites has been extensively studied in past decades (McArthur and Walsh, 1984; Watkins et al., 1995; Zhu et al., 2014; Joosu et al., 2015; Emsbo et al., 2015; Auer et al., 2017; Shields and Stille, 2001; Shields and Webb, 2004). While

the seawater REE+Y concentrations are only at µg/kg level (Zhang and Nozaki, 1996), the REE+Y abundances in both bioapatites and sedimentary phosphorites are several orders of magnitude higher (e.g., Chen et al., 2015; Emsbo et al., 2015). This can be, most likely, attributed to the dissolution of the REE+Y-scavenging phases, such as organic matter, clay minerals or Fe-Mn oxyhydroxides, in the diagenetic environment where apatite forms, resulting in significantly higher REE+Y concentrations in pore-water compared to seawater (Elderfield and Sholkovitz, 1987; Haley et al., 2004; Abbott et al., 2015). Given the elevated apatite REE+Y concentrations compared to seawater, and that Recent phosphorites are depleted in REE+Y compared to pre-Quaternary phosphorites (McArthur and Walsh, 1984), it has been proposed that REE+Y uptake occurs mainly in the diagenetic environment, where the pore-water chemistry can be significantly different from seawater (Haley et al., 2004).

It is curious that Late Mesozoic to Recent sedimentary phosphorites show seawater-like patterns with small negative Ce anomalies and HREE enrichment (Shields and Stille, 2001; Emsbo et al., 2015), whereas older phosphorites exhibit negative Ce anomalies, but no HREE enrichment (Shields and Stille, 2001). This apparent secular variation in phosphorite REE+Y patterns has been attributed either to changes in seawater chemical composition or to the variation of sedimentary settings, burial depth and post-depositional uptake and ion exchange (Shields and Webb, 2004; Emsbo et al., 2015). Emsbo et al. (2015) showed that phosphorites from the same time period, but from different sedimentary settings and burial depth, show remarkably similar REE patterns. While a strong case can be made for secular variation of ocean water chemistry, a cause for this change is unknown and without a clear theoretical basis. Moreover, the REE+Y patterns of Phanerozoic non-phosphatic authigenic marine sediments are similar to modern day seawater and show no apparent secular variation (Shields and Webb, 2004) – thus, the use of sedimentary REE+Y patterns as robust proxies of seawater compositions and redox states remains controversial.

In this contribution we focus on well-characterized Recent sedimentary phosphorites on the Namibian shelf of the Atlantic Ocean, the formation of which is fueled by the Benguela Upwelling System. The aim of this contribution was to (a) study the REE+Y composition of modern sedimentary apatites from the Namibian shelf, and (b) assess the degree of the diagenetic overprinting on the primary REE+Y signatures.

2. Geological setting

The sedimentary phosphorite deposits of the Namibian and South African shelves were first discovered in the 19th century during the HMS *Challenger* expedition (Murray and Renard, 1891), and their formation and economic potential has attracted attention since then (Coles et al., 2002). Phosphogenesis on the Namibian shelf is a complex phenomenon involving microbially mediated Ca-phosphate precipitation (Schulz and Schulz, 2005) and mechanical concentration of apatitic grains by sediment reworking and winnowing caused by changes in sea level (Compton and Bergh, 2016). It is also notable that *Thiomargarita namibiensis* – a large sulphur-oxidizing bacterium – was first discovered in the sediments of the Namibian shelf (Schulz et al., 1999). These bacteria control the phosphate levels in pore-water and possibly trigger the formation of sedimentary phosphorites (Schulz and Schulz, 2005).

The Namibian shelf is composed of Precambrian basement rocks topped with a relatively thin unit of seaward dipping Cretaceous to Cenozoic sedimentary deposits overlain by Pleistocene to Recent sediment cover (Compton and Bergh, 2016). The shelf is unusually broad (up to 150 km wide; Brüchert et al., 2006) and extends to 400 m water depth (Compton and Bergh, 2016). It is divided into three zones: the inner shelf, water depths up to 130 m; the middle shelf, up to 300 m; and the outer shelf, depths up to 400-500 m.

The entire southwestern African shelf and especially its Namibian section is influenced by one of the strongest upwelling zones in the world, known as the Benguela Upwelling System (Goldhammer et al., 2011). The Benguela Upwelling System delivers nutrient rich cold water to the surface, causing extremely high biological productivity, which, in turn, leads to large scale organic carbon burial (Inthorn et al., 2006). The accumulation of organic carbon and algal debris has formed a 14-m-thick layer of organic rich diatomaceous ooze which extends over 700 km along the inner shelf (Emeis et al., 2004). Nearshore (water depths <50 m), the sediment cover is mainly made up of sand and gravel, middle to outer shelf sediments largely consist of phosphorite sand, whereas the outermost shelf and slope sediments are carbonates (Figure 1; Compton and Bergh, 2016).

An increased flux of sinking organic matter due to intense upwelling, coupled with shallow water depth, are the main factors enabling the formation of sedimentary phosphorites on the Namibian shelf. Intense upwelling during seawater highstands promotes precipitation of apatitic

concretions on the inner shelf (Compton and Bergh, 2016; Mänd et al., 2018). The active region of phosphogenesis is thought to be primarily located on the inner shelf, near Walvis Bay, while older phosphorite deposits can be found further south (Compton et al., 2002; Compton and Bergh, 2016).

Principally, two distinctive types of sedimentary apatitic grains can be distinguished on the Namibian shelf: (a) authigenic, concretionary apatitic grains occurring in the pore-space of sediments of the inner shelf and (b) reworked and redeposited, pelletal apatitic grains on the middle and outer shelf (Compton and Bergh, 2016). Based on strontium isotope stratigraphy, the oldest redeposited pelletal phosphorites are roughly 5.8 Ma old, with the most intense episodes of phosphogenesis having taken place during Pliocene and Pleistocene (Compton and Bergh, 2016), and the youngest concretionary apatites being late Pleistocene to early Holocene in age (Baturin, 2000). During reworking, apatitic concretions are rounded to form pelletal apatitic grains. Variable grain size and intragranular zonation has been described in some of the pelletal grains suggesting multiple episodes of phosphogenesis (Baturin, 2000). Pelletal and concretionary apatitic grains make up 80-90% of phosphorite deposits, while the rest is made up of fish remains, mollusc molds, phosphatized calcareous fossils and recent phosphatic brachiopods (Baturin, 2000; Compton and Bergh, 2016).

3. Material and methods

The sediment samples were collected in May 2015 during an oceanographic cruise on-board the R/V Mirabilis. An Ocean Instruments MC-400 multi-core was used to retrieve the sediment cores. Two cores containing sedimentary apatite were used in this study: CG4 (~300 m b.s.l., core length 21 cm, containing pelletal apatitic grains) and 25005 (~50 m b.s.l., 25 cm in length, containing concretionary apatitic grains; Figure 1). The cores were sectioned and sampled at 1 cm intervals for the uppermost 10 cm and at 2 cm intervals below 10 cm sediment depth. After sectioning, the samples were freeze dried.

Apatitic grains were handpicked from bulk samples under a light microscope, cleaned in an ultrasonic bath and mounted on scanning electron microscope stubs. The grains were embedded in Technovit® EPOX epoxy-resin and ground down and polished to reveal the cross-section of the grain. Leica EMRES101 Wide Beam Argon Ion Mill was used to produce a flat and clean surface of the samples. The structure and elemental composition of the cross-sections were

analyzed using a variable pressure Zeiss EVO MA15 scanning electron microscope (SEM) equipped with an Oxford X-MAX energy dispersive detector system (EDS) and Aztec software (version 3.1) for element analysis.

The REE+Y concentrations in apatitic grains were measured by laser ablation inductively coupled plasma mass spectrometry (LA-ICP-MS) using an Agilent 8800 quadrupole ICP-MS coupled to a Cetac LSX-213 G2+ laser with HelEx II fast-washout two-volume large-format cell. Helium at a combined flow rate of 0.8 l/min was used as a carrier gas in the laser and was mixed with argon (0.9 l/min) downstream of the cell. Elemental concentrations were calculated from raw spectrometry data using ^{43}Ca as an internal standard, assuming stoichiometric apatite Ca concentration (39.7%). Additionally, the GSD-1G certified reference material, using values from Jochum et al. (2011), was used as an external calibration standard. BCR-2G was used as a quality control standard. For mapping and line scan measurements, a spot size of 10 μm with a scan speed of 2 μm/s, at 5 Hz and a fluence of 1.65 J/cm^2 was used. Spot measurements of the central part of apatitic grains were performed using a spot size of 50 μm with a shot count of 40 s, at 10 Hz and a fluence of 1.1 J/cm^2, whereas the ablation parameters were 25 μm, 40 s, 10 Hz and 1.65 J/cm^2 for the exterior of the apatites. Signals of ^{27}Al, ^{31}P and ^{43}Ca were used to monitor for possible clay contamination. Samples containing >20000 mg/kg of Al were discarded from the dataset.

For LA-ICP-MS mapping and line scans, the following masses were measured: ^{27}Al, ^{34}S, ^{43}Ca, ^{57}Fe, ^{89}Y, ^{137}Ba, ^{139}La, ^{140}Ce, ^{141}Pr, ^{147}Sm, ^{153}Eu, ^{165}Ho, ^{172}Yb, ^{232}Th and ^{238}U. For line scan analysis, the GSD-1G standard was measured twice per 5 line scans, while the external standard was measured 3 times before and after mapping. Minimum detection limits, calculated from repeated analysis of the GSD-1G standard, were below 0.5 mg/kg for all REE+Y. During measurements the deviation of measured REE+Y concentrations from reference values given for BCR-2G standard were on average <20%. The relative standard deviation (RSD) value was 5% for most of the elements, except for Eu, Ho and Yb (RSD <20%).

The following isotopes were measured during spot analysis: ^{27}Al, ^{31}P, ^{34}S, ^{43}Ca, ^{88}Sr, ^{89}Y, ^{137}Ba, ^{139}La, ^{140}Ce, ^{141}Pr,^{146}Nd, ^{147}Sm, ^{153}Eu, ^{157}Gd, ^{159}Tb, ^{163}Dy, ^{165}Ho, ^{166}Er, ^{169}Tm, ^{172}Yb, ^{175}Lu, ^{232}Th and ^{238}U. For spot analysis, the GSD-1G standard was measured 2 times per 20 samples. Detection limits, calculated from the external standard, were 0.5 mg/kg for Gd and below 0.1

mg/kg for the other REE+Y. The average deviation of the measured BCR-2G concentrations from the reference values was <5%, and RSD was 1-10% for all REE+Y. Measured REE concentrations were normalized against Post Archean Average Shale (PAAS; Taylor and McLennan, 1985). Ce, Eu, Pr and Y anomalies were calculated as: $Ce/Ce^* = Ce_N/(0.5La_N+0.5Pr_N)$, $Eu/Eu^* = Eu_N/((Sm_N+Gd_N)/2)$, $Pr/Pr^* = Pr_N/(0.5Ce_N+0.5Nd_N)$ and $Y/Y^* = Y_N/((Dy_N+Ho_N)/2)$ (Bau and Dulski, 1996, Byrne and Sholkovitz, 1996), Y/Ho ratios were calculated using measured values in mg/kg.

The studied samples were not directly dated. The ages of both concretionary and pelletal apatitic grains were estimated based on age relationships established by Baturin (2000) and Compton and Bergh (2016)"

4. Results

4.1. Microscopy

Concretionary apatitic grains from core 25005 measure 50-300 µm in size, are dark gray or black in color and subangular to poorly rounded in shape. Their surfaces are usually irregular and pitted. Fossil debris – mainly diatom frustules – and terrigenous mineral grain inclusions are abundant in the grains (Figure 2a-b), while sulphur containing minerals are scarce in the grains from this core (Figure 3). The average size of pelletal apatitic grains in core CG4 is larger, varying from 200 µm to 500 µm (Figure 2c-f). Under an optical microscope, the grains are dark in color, well rounded, spherical in shape and with smooth surfaces. Their interiors contain inclusions of barite and pyrite, often as casts diatom and other fossil molds (Figure 2d, 4). Concretionary apatitic grains from core 25005 are more porous than pelletal grains from core CG4, and some pelletal grains show concentric layering with multiple episodes of apatite growth (Figure 2e). Elemental mapping of apatitic grains shows no significant intragranular variations of Ca or P in either of the cores, whereas sulphur content varies both between different grains and intragranularly (Figure 2a-f).

4.2. LA-ICP-MS

Pelletal apatitic grains from core CG4 have higher REE+Y concentrations than the concretionary grains from core 25005: average apatite ∑REE+Y content in grains from core 25005 is 448 mg/kg and 846 mg/kg in core CG4. No significant correlation between REE+Y content and

sample depth is present (Figure 5). Distribution of REE+Y concentrations within studied grains is concentrically zoned. In the central parts of the grains the ∑REE+Y ranges from 3 to 394 mg/kg in concretionary grains and from 1 to 455 mg/kg in pelletal grains, whereas in the exterior layers of the grains the average ∑REE+Y contents are 658 and 1621 mg/kg, respectively (Figures 6, 7). Such "enrichment zone" is characteristic to all of the grains measured. The width of this zone varies between different grains, but rarely exceeds 20 µm (Figures 6, 7, 8).

PAAS normalized REE+Y patterns can be divided into four types: (a) modern seawater patterns with high (>50) Y/Ho ratios, negative Ce anomalies and HREE enrichment that are mostly found in the central parts of concretionary apatitic grains (Figure 9b); (b) HREE enriched patterns, with Y/Ho ratios around or slightly below modern seawater values and slightly negative to no Ce anomalies found in the central parts of pelletal apatitic grains (Figure 9a); (c) patterns with no Ce anomaly, modest HREE enrichment characteristic to the enrichment zone of concretionary apatitic grains (Figure 9d); and (d) flat patterns, with minor LREE depletion and no or slightly positive Ce anomalies that are found in the outer layers of the pelletal grains (Figure 9c).

None of the apatite grains measured show a positive or negative Eu anomaly. Eu/Eu* values remain constant (0.9-1.1) in both cores. Ce/Ce* values show significant variability, ranging from 0.5 to 1.15 (Figure 10). Average Ce/Ce* ratios in concretionary grains and in the central parts of the pelletal grains are around 0.6-0.9 whereas within the outer enriched zone of the pelletal grains the values are higher than 0.9, often >1. Y/Ho values show a systematic decrease from more pristine grains towards more mature and reworked grains. The highest Y/Ho values of >50 are found in the central parts of the apatitic grains of both types. The Y/Ho values in the enrichment zone in concretionary grains are around 50 to 40 but are as low as 30 in pelletal grains (Figure 11). La_N/Yb_N values are higher in pelletal grains (0.5-0.9 in the center, 0.4-0.6 in the enrichment zone), whereas in the concretionary grains, the La_N/Yb_N values range from 0.2-0.4 throughout the whole grain (Figure 12a). La_N/Sm_N ratios are lower in the enrichment zone of both grain types, averaging around 0.6, while the central parts of both pelletal and concretionary apatitic grains show more variability, with values ranging from 0.5 to 2.1. The majority of the measured samples are in the range of modern seawater La_N/Yb_N and La_N/Sm_N values, except in the enrichment zones and in some of the central parts of the pelletal grains from core CG4. Y/Y* and La_N/Nd_N ratios are the lowest in the enrichment zone of grains from core CG4 and highest in

the concretionary grains from core 25005 (Figure 12b). The enrichment zones of both concretionary and pelletal apatitic grains have a rather coherent REE+Y composition and show little variability, while the REE+Y concentrations in central part of both types of grains are somewhat different (Figures 10, 12).

Uranium is rather abundant both in concretionary and pelletal apatitic grains (Figures 6, 7). Average U content in the central parts of the apatitic grains is 40 mg/kg in the concretionary grains and 56 mg/kg in the pellets. Th is less abundant in the internal part of both grain types, with concentrations of 0.7 mg/kg and 1.2 mg/kg respectively. Both U and Th are heavily enriched in the exteriors of the apatitic grains, with average concentrations as high as 152 mg/kg of U and 41 mg/kg of Th. The enrichment zones of pelletal apatitic grains contain more Th and U than the concretionary apatite grains.

5. Discussion

5.1 REE+Y distribution

Watkins et al. (1995) reported REE values (without Ho, Tm and Lu) ranging between 10-1350 mg/kg and flat-shaped shale-like patterns in bulk Namibian phosphorites. Our data, however, show distinctive differences in REE+Y composition both in terms of concentrations and PAAS normalized REE+Y patterns in concretionary and pelletal apatitic grains in the Namibian shelf. Our results show REE+Y enrichment zones at grain margins that are consistent with the model described by McArthur and Walsh (1984) which suggests that during precipitation apatite contains very low abundance of REE+Y and that the majority of these elements are incorporated during subsequent diagenetic pore water-mineral interactions. The width of enrichment zones varies from 10 to 20 µm in different grains (Figures 6, 7). There is no clear correlation between sample depth and REE+Y concentrations in the studied grains (Figure 5), and the extent of these zones is likely dictated by the surface area to mass ratios of the apatite grains. Furthermore, the enrichment zones of older, reworked pelletal grains do not appear to be systematically wider than the REE+Y-enriched zones in concretionary apatitic grains. Instead, the exteriors of apatitic grains seem to take up REE+Y continuously, causing cumulatively higher degrees of enrichment, but the width of zone itself stays within 10-20 µm, suggesting an inhibited diffusion and ion-exchange between the pore-water and the grains interiors.

The uptake of REE+Y by apatite is likely limited by the availability of these elements in shallow pore-water (McArthur and Walsh, 1984; Haley et al., 2004; Abbott et al., 2015). Seawater itself has very low REE concentrations ranging from 20-220 pmol/kg in different oceanic basins and depth-zones through the water-column (e.g., Elderfield and Greaves, 1982; De Baar et al., 1985; Alibo and Nozaki, 1999; Wang and Yamada, 2007; Garcia-Solsona et al., 2014; Deng et al., 2017; de Baar et al., 2018). Pore-waters, however, may have two orders of magnitude higher REE+Y abundances compared to seawater, mainly as a result of the degradation of organic matter and the dissolution of Fe-Mn oxyhydroxides, which carry adsorbed REE+Y into the sediments (Haley et al., 2004; Abbot et al., 2015). The pore-water in the very uppermost few-centimeters-thick layer of sediment near the seawater–sediment interface shows the highest REE+Y enrichment whereas the shallow subsurface pore-water below that zone shows a rapid decline in ΣREE+Y concentration, which has been interpreted to reflect the decrease of REE+Y release from organic matter, Fe-Mn oxyhydroxides, and detrital components, or the increase of REE+Y removal (Haley et al., 2004; Deng et al., 2017).

This uppermost few centimeters of sediment at the seafloor is also the zone where phosphogenesis takes place. Studying the organic-rich sediments off the Namibian coast, Schulz and Schulz (2005) reported that the ~3-cm-thick horizon had phosphate concentrations of up to 300 µM in the pore-water and ~25% of hydroxyapatite in the solid phase. Mänd et al. (2018) data on the core 25005 studied here, demonstrated an increasing apatite abundance from ~4 wt.% at the sediment surface to 9-11 wt.% at 6 cm depth followed by a decline to ~1-3 wt.% at 10 cm depth and to <1 wt.% further down.

Notably the REE+Y enrichment in the outermost zone of the apatitic grains overlaps with the elevated concentrations of Th and U. It is established that modern sedimentary apatites are enriched in U and Th (Baturin and Dubinchuk, 2005; Arning et al., 2009b; Brock and Schulz-Vogt, 2011). The enrichment of redox sensitive U via the reduction of soluble U^{+6} to insoluble U^{+4} takes place under suboxic conditions and is possibly amplified by slow sedimentation rates on the Namibian shelf that allows U diffusion from the water column to the sediments (Tribovillard et al., 2006). Whereas Th is not a redox sensitive element and less soluble in seawater compared to U, the removal of Th from the water column is coupled with the redox cycle of Fe-Mn particles. During early diagenesis, particle bound Th is released to pore-water

(Abanda and Hannigan, 2006), from where it is scavenged by apatite, possibly also as a Th-phosphate particulate phase (Rigali et al., 2016).

Concentrically layered pelletal apatitic grains (Figure 7) suggest a complex post-depositional diagenetic development and a reactivation of apatite precipitation over time. The central parts of the grains, which are likely remnants of pristine concretionary apatite, are commonly somewhat porous, containing barite cast after diatom molds, and characterized by low REE+Y concentrations. Such cores are surrounded by pyritized zones/lamellas that are marked by REE+Y enrichment compared with the central parts of the grains. The REE+Y enriched zones are not as sharp and enriched with respect to REE+Y as the outermost zone but were likely developed due to pore water - pellets interaction during breaks in phosphate precipitation. Given the rapid nature of apatite nucleation and crystal growth in Namibian apatitic grains (Mänd et al., 2018) we can suggest that these breaks in active phosphate precipitation were probably not long enough to allow significant REE+Y uptake.

Repetition of such concentric apatite and pyritized zones with REE+Y enriched margins points to multiple episodes of crystal growth under changing redox conditions (Arning et al., 2009b). Phosphate precipitation at upwelling sites is interpreted to occur at sharp fluctuating redoxclines in shallow subsurface sediments (Ruttenberg and Berner, 1993; Brock and Schulz-Vogt, 2011). Sulphur-oxidizing bacteria such as *Thiomargarita namibiensis*, which inhabit these sediments in large numbers (Schulz and Schulz, 2005), are capable of storing polyphosphate during oxic-suboxic conditions and metabolizing/releasing the phosphate under sulfidic conditions, supersaturating the pore-water with respect to Ca-phosphate (Arning et al., 2009a; Goldhammer et al., 2010). Though recent studies have shown that *Thiomargarita* spp. are not the only contributors to changing phosphate concentrations that might lead to phosphogenesis (Zoss et al., 2018), the zoned inner structure of phosphatic pellets agrees well with the periodic growth of the apatitic grains under fluctuating redox conditions, implying that the zonal enrichment of Th, U and REE+Y, particularly in the external layers of the apatitic grains, is likely caused by uptake of these elements during predominantly suboxic-sulfidic pore-water conditions after the initial formation and burial of apatitic concretions. This also suggests that if the apatite grains are not subjected to late stage recrystallization, the intragranular distribution and concentrations of REE+Y can provide insight into the changes in redox conditions during the growth and

diagenesis of the apatitic pellets. REE+Y abundance and distribution in apatitic grains should, thus, reflect the REE+Y concentration and composition of seawater and/or shallow pore-water in the central parts of the apatitic grains whereas the REE+Y composition in the enrichment zones reflects the changing pore-water composition during diagenesis.

5.2 REE+Y patterns

The modern oxygenated seawater REE+Y patterns are characterized by negative Ce anomaly, positive Y anomaly and HREE enrichment (Bau et al., 2010; Shields and Webb, 2004). However, earlier reported REE patterns of Namibian apatites, measured from bulk digested samples, were characterized by flat, shale-like patterns without negative Ce-anomaly (McArthur and Walsh, 1984; Watkins et al. 1995) and were interpreted as being diagenetic and not reflective of the overlying seawater chemistry (Watkins et al., 1995). Our spatially resolved laser ablation measurements, however, reveal contrastingly different REE+Y patterns from the interiors and exteriors of the Namibian apatitic grains.

The PAAS-normalized REE+Y patterns of apatite in the cores of concretionary grains are similar to modern seawater (de Baar et al., 1985) characterized by a progressive enrichment toward HREE, a depletion in Ce, slight enrichment in Gd (related to the gradual filling of the 4f-orbital across the lanthanide series, which causes increased stability of some elements; Masuda and Ikeuchi, 1979; Bau, 1999), and strong enrichment in Y (Figure 9b). The central parts of the pelletal grains show slightly higher REE+Y concentrations compared with the concretionary grains but the PAAS normalized patterns indicate, in most cases, the preservation of only a slight Ce depletion (but in rare cases show a positive Ce anomaly), whereas Gd enrichment is subdued or absent. The patterns are flattened towards the HREE though strong Y enrichment is still present (Figure 9a). The outermost REE+Y enriched zones in both grain types show flattened REE+Y patterns with enrichment in LREE and MREE relative to the inner parts of the grains and no or only slight enrichment in Ce. Even in concretionary grains only in few cases a weak Ce depletion is apparent in the enrichment zones. Also, the outermost REE+Y rich zones are characterized by a significantly diminished enrichment in Y (Figure 9c, d). Though differences remain between the core and the outermost enriched zone, this indicates that in pelletal apatitic grains at least some degree of diagenetic ion exchange has occurred between the interior and exterior of the grains, and pore-water during diagenesis.

Modern seawater carries a negative Ce anomaly because under oxic seawater conditions Ce^{+3} is oxidized to Ce^{+4} and becomes preferentially scavenged by Fe-Mn oxyhydroxides and organic particles leaving the seawater depleted of Ce compared to neighboring elements La and Pr (Byrne and Sholkovitz, 1996). Therefore, sediments precipitating from oxic seawater record this characteristic Ce depletion. In stratified water-bodies with well-developed redoxclines (e.g. in the Black Sea), this anomaly becomes increasingly negative with water depth until the redoxcline, where it sharply diminishes due to the reduction of Ce^{4+} to soluble Ce^{3+} as the environment becomes anoxic (Ling et al., 2013). In addition to oxidation state, Ce depletion in seawater is affected by pH, water depth, the age of the seawater body (Shields and Stille, 2001; Pattan et al., 2005) and by microbial activity that catalyzes the oxidation of Ce^{3+} (Moffett, 1990). A true negative Ce anomaly – defined by Ce/Ce* <1 and Pr/Pr* > 1 (sensu Bau and Dulski, 1996) – can be identified only in about one third to one quarter of samples measured. These true negative Ce anomalies, found in the central parts of concretionary and pelletal apatitic grains (and in some cases in outer parts of the concretionary grains), suggest a oxic seawater environment during their formation. (Figure 10, field IIIb). Intriguingly, the enrichment zones, particularly in the reworked grains, show a true positive Ce anomaly (Figure 10, field IIIa). The positive Ce anomaly indicates uptake of REE+Y released by reductive dissolution of Mn^{4+} oxides under anoxic conditions (Takahashi et al., 2015).

The PAAS normalized REE+Y patterns of pore-waters in shallow marine sediments are characterized by a flat pattern, absence of a negative Ce anomaly and a slight increase in HREE and MREE (Sholkovitz et al., 1989; Haley et al., 2004; Kim et al., 2012; Abbott et al., 2015; Deng et al., 2017). The principal shape of PAAS normalized pore-water patterns varies with the location on the shelf (margin to slope and basin) as well as the sampling depth within the sediments (shallow – deep pore-water; Haley et al., 2004; Deng et al., 2017). Further, Haley et al. (2004) have suggested that patterns in the ferruginous zone of anoxic sediments are characterized by MREE enrichments whereas anoxic pore-water deeper in the sediments within the sulfidic and methanogenic zones shows a flat PAAS normalized pattern or a slight HREE enrichment (Haley et al., 2004; Kim et al., 2012). Phosphatic minerals are particularly prone to MREE uptake (Byrne et al., 1996) due to higher similarity between the ionic radii of Ca and MREE (Reynard et al., 1999). In the outermost enrichment zones of the Namibian apatitic grains the MREE enrichment is not that obvious. However, it is evident that the REE+Y uptake occurs

in the anoxic zone of the shallow sediments where REE+Y are released from particulate carriers probably causing progressive removal of REE+Y from the pore-water deeper in the sediment column (Haley et al., 2004; Kim et al., 2012; Abbot et al., 2015, Deng et al., 2017).

5.3 Y/Ho ratio

Yttrium behaviour is similar to redox-insensitive REEs, especially to Ho, its geochemical twin with identical valence and nearly the same ionic radii. Therefore, Y and Ho are coupled in geochemical processes resulting in a constant Y/Ho ratio of 28 in chondritic materials and igneous rocks (Bau and Dulski, 1996). However, due to the higher affinity of Ho towards Fe-Mn oxyhydroxides (Bau and Dulski 1994), Y is enriched in oxygenated seawater and super-chondritic Y/Ho values are measured in modern oceans with a typical ratio above 52 (Nozaki et al., 1997). Y/Ho ratios of >50 are characteristic to the central parts of the apatitic grains of both types (Figure 11), and are unequivocally in unison with REE+Y patterns from grain cores suggesting the nucleation of Namibian apatitic grains in equilibrium with seawater. This interpretation is further supported by La_N/Yb_N and La_N/Sm_N ratios measured in the center of the pristine concretions that plot on the field of modern seawater (Figure 12a). In contrast, Y/Ho ratios are significantly lower in the exteriors of the apatitic grains of both types, reaching values of ~30 in the enrichment zones of pelletal grains. This is accompanied by a gradual increase in Sm_N/Yb_N values indicating increasing dominance of MREE relative to HREE in the enrichment zones of the apatitic grains (Figure 11). The original signature inherited from seawater is evidently overprinted within the sediment below the shallow redoxcline where particulate bound Ho (and MREE) is released back to the pore-water during redox cycling (Bau et al., 1997), thus lowering the Y/Ho ratio of the fluid interacting with apatitic grains.

Moreover, the diagenetic origin of the outermost REE+Y-enriched zones is hinted at by the La_N/Yb_N and La_N/Sm_N ratios. Reynard et al. (1999) have suggested that La_N/Yb_N ratios are not affected during diagenesis if REE+Y uptake is governed by substitution and that La_N/Sm_N ratios remain unaffected if uptake occurs by adsorption. Although slightly lowered La_N/Sm_N values imply the presence of a substitution mechanism, possibly increasing with the advancement of diagenesis, elevated La_N/Yb_N ratios of the outermost REE+Y-enriched zones (compared with typical seawater values of 0.2-0.5; Figure 12a) suggest adsorption as the main mechanism of REE+Y uptake during early diagenesis near the seawater-sediment interface, particularly in

pelletal grains (Reynard et al., 1999). Furthermore, the systematic decrease of Y/Y* and La_N/Nd_N ratios from pristine concretions to the rims of the pelletal apatitic grains is in accordance with the diagenetic development of the apatitic grains on the Namibian shelf, as Y/Y* and La_N/Nd_N values are expected to decrease progressively during diagenesis (Shields and Stille, 2001).

5.4 Implications to phosphogenesis and REE+Y uptake

The majority of modern sedimentary phosphorites are formed on the continental shelves of Namibia, Peru, the Arabian Sea and Baja California, where upwelling of nutrient rich deep water leads to high primary productivity, which in turn, leads to high rates of organic carbon burial (Fölmi, 1996). Precipitation of sedimentary apatite in the uppermost layer of the sediment requires that pore-water becomes supersaturated with respect to dissolved phosphate species (Föllmi, 1996). Degradation of organic matter by microbially mediated reactions (predominantly sulphate reduction; Glenn et al., 1994; Arning et al., 2009a), the transport and release of phosphate adsorbed onto Fe-Mn oxyhydroxides under oscillating redox conditions (Pufahl and Grimm, 2003), and the repeated mixing of iron phases over the redox boundary by bioturbation (Jarvis et al., 1994) have traditionally been considered as the main processes building up interstitial phosphate concentrations needed for apatite precipitation. To maintain this supersaturation at least some pore-space restriction is required. Also, the activity of sulphur bacteria *Thiomargarita* spp., *Beggiatoia* spp. and *Thioploca* spp. can influence the pore-water phosphate concentrations as these microbes engage in "bacterial pumping" of phosphate into their surrounding pore space through their polyphosphate metabolism (Schulz and Schulz, 2005). Collectively, the interplay of variety of processes occurring in shallow subsurface sediments can lead to pore-water supersaturation with respect to Ca-phosphate, precipitation of which is facilitated by presence of microbially-produced organic matter acting as nucleation templates for the apatite precursor phases (Mänd et al., 2018). Except for "bacterial pumping", the transport and release of REE+Y into pore-water is principally governed by the same mechanisms (organic matter degradation and Fe-Mn oxyhydroxides reduction), so that phosphate and REE buildup in the uppermost few-centimeters-thick layer just below the sediment-water interface seems to be paired (Schulz and Schulz, 2005; Haley et al., 2004; Deng et al., 2017). However, the low REE+Y concentrations and the seawater-like PAAS normalized patterns in studied apatitic

grains show that the initial phosphate nucleation on the Namibian shelf occurs in a normal seawater controlled environment not in shallow pore-water with elevated REE+Y concentrations and flattened or MREE bulging patterns (e.g., Haley et al., 2004; Deng et al., 2017).

It can, therefore, be suggested that the release of phosphorus and Ca-phosphate supersaturation/nucleation occurs before the REE+Y inventory of the pore-water becomes dominated by REE+Y released from degradation of organic material and reductive dissolution of Fe-Mn oxyhydroxides, possibly within giant sulphur bacterial mats (Figure 13) at the expense of phosphate liberated from bacterial polyphosphate hydrolysis (Schulz and Schulz, 2005; Brock and Schulz-Vogt, 2011). Sulphur bacteria on the Namibian shelf form extensive bacterial mats with a reported biomass of nearly 50 g m^{-2} (Schulz et al., 1999). Sulphide-oxidizing bacteria of the genera *Thiomargarita* and *Beggiatoa*, which occupy the (sub)oxic-sulfidic sediment interface, gain energy under (sub)oxic conditions from the oxidation of H_2S and other reduced sulphur species using O_2 or NO_3^-, while accumulating polyphosphate and nitrate from seawater in the vacuole structures of their large cells (Schulz and Schulz, 2005; Brock and Schulz-Vogt, 2011). The phosphorus that is stored and metabolized by bacteria is thus decoupled from REE+Y transport-release processes and bears seawater-like REE+Y patterns (Figure 12) that are similar to that of authigenic carbonate minerals precipitating from seawater (e.g., Li et al., 2019).

REE+Y uptake continues after initial nucleation and growth, and when grains become enclosed/buried within the sediment the REE+Y signatures record the changing pore-water composition, though this is restricted to the outermost zone of the apatitic grains. While the behavior of REE+Y in pore-waters is likely dependent on more parameters than merely changes in redox conditions (e.g., Abbot et al., 2015), early diagenetic uptake of REE+Y in Namibian apatitic grains seems to be primarily driven by the reductive dissolution of Fe-Mn oxyhydroxides and organic matter under suboxic-sulfidic conditions. Although the cores of the apatitic grains do not become significantly enriched in REE+Y, small scale adsorption-desorption processes still occur, slowly overprinting the primary seawater-like pattern, lowering the Y/Ho and raising the Ce/Ce*, La_N/Yb_N ratios.

The universal nature of such early diagenetic REE+Y enrichment at the surface of authigenic particles like the Namibian apatitic grains is further underlined by a very similar authigenic-diagenetic REE enrichment process recently reported on Holocene to Recent planktonic

foraminifer surfaces from the Iberian margin of the Atlantic Ocean (Skinner et al., 2018). The authors show that primary seawater signatures recorded in foraminifer shells become overprinted due to early diagenetic interaction with pore-fluids leading to the formation of coatings that are enriched with respect to LREE and MREEs, whereas the amplitude of Ce-anomalies was found to diminish with advancing burial and the onset of anoxic conditions in the sediment.

Our results undermine the usefulness of authigenic sedimentary phosphorites as a potential archive of the past seawater, particularly its redox state and secular changes (e.g., Lecuyer et al., 2004; Emsbo et al., 2015). Bulk analysis of sedimentary phosphorites would result in erroneous conclusions on the redox status of their depositional environments, unless a careful screening and a detailed characterization of the compositional variations within the apatitic grains and/or crusts is performed using *in-situ* analytical methods of choice.

6. Conclusions

Our study shows that the two distinctive types of sedimentary apatitic grains on the Namibian shelf, authigenic concretions and reworked and redeposited pellets, both have distinct variation in their REE+Y composition. The REE+Y are concentrated in the external layers of the grains, forming a 10-20 μm wide "enrichment zone", while the interior parts of both concretionary and pelletal apatitic grains are low in REE+Y. A general trend of increasing REE+Y concentrations in this enrichment zone with increasing maturity is apparent when comparing the two grain types indicating continuing REE+Y uptake in sedimentary apatite.

PAAS-normalized REE+Y patterns; Y/Ho, La_N/Yb_N, ratios and Ce/Ce* values; and Y enrichment in the cores of apatitic grains all bear seawater-like characteristics, though in many pelletal grains the values are shifted outside the range of modern seawater. The REE+Y enriched zones in both grain types show flattened REE+Y patterns with enrichment in LREE and MREE relative to the inner parts of the grains, no or only slightly positive Ce/Ce* values and diminished or absent Y enrichment.

The seawater-like REE+Y characteristics of the phosphate grain nuclei suggest their precipitation in equilibrium with seawater, possibly within bacterial mats of giant sulphur bacteria that are abundant in the Namibian upwelling systems and that control phosphogenesis through bacterial phosphate pumping. REE+Y enrichment on grain margins occurs during post-

depositional adsorption-desorption processes and the respective REE+Y signals reflect the composition and development of pore-water, not seawater.

Given the preferential scavenging of REE+Y by apatite, when compared to other marine authigenic minerals, slight changes in pore-water compositions can easily affect the primary signatures of sedimentary apatites. The Namibian apatites, while relatively young on a geological timescale, are already significantly altered in terms of their REE+Y concentrations and patterns. Overprinting of primary signatures thus occurs relatively early after precipitation and the usefulness of apatite REE+Y patterns as proxies for past seawater conditions remains questionable, particularly when bulk analysis is applied. The thin layer of REE+Y enrichment at the surface of apatitic grains forms during post-depositional uptake, but accounts for the majority of REE+Y content. Because of the significant variation in intragranular distribution of REE+Y in sedimentary apatite the use of micro-scale laser ablation is preferable to acid digestion when studying phosphatic marine sediments.

Acknowledgments

We would like to thank the organizers and participants of the Regional Graduate Network in Oceanography Discovery Camp 2015, funded by the Agouron Institute and the Scientific Committee for Oceanographic Research (SCOR); the captain and crew of R/V Mirabilis and the University of Namibia for access to coring sites and help with sample gathering. This study was supported by Estonian Science Agency project PRG447 and Estonian Centre of Analytical Chemistry.

References

Abanda P. A. and Hannigan R. E. (2006) Effect of diagenesis on trace element partitioning in shales. *Chem. Geol.* **230**, 42–59.

Abbott A. N., Haley B. A., McManus J. and Reimers C. E. (2015) The sedimentary flux of dissolved rare earth elements to the ocean. *Geochim. Cosmochim. Acta* **154**, 186–200. Available at: http://dx.doi.org/10.1016/j.gca.2015.01.010.

Alibo D. S. and Nozaki Y. (1999) Rare earth elements in seawater: Particle association, shale-normalization, and Ce oxidation. *Geochim. Cosmochim. Acta* **63**, 363–372.

Arning E. T., Birgel D., Brunner B. and Peckmann J. (2009a) Bacterial formation of phosphatic laminites off Peru. *Geobiology* **7**, 295–307.

Arning E. T., Lückge A., Breuer C., Gussone N., Birgel D. and Peckmann J. (2009b) Genesis of phosphorite crusts off Peru. *Mar. Geol.* **262**, 68–81. Available at: http://dx.doi.org/10.1016/j.margeo.2009.03.006.

Auer G., Reuter M., Hauzenberger C. A. and Piller W. E. (2017) The impact of transport processes on rare earth element patterns in marine authigenic and biogenic phosphates. *Geochim. Cosmochim. Acta* **203**, 140–156. Available at: http://dx.doi.org/10.1016/j.gca.2017.01.001.

Azmy K., Brand U., Sylvester P., Gleeson S. A., Logan A. and Bitner M. A. (2011) Biogenic and abiogenic low-Mg calcite (bLMC and aLMC): Evaluation of seawater-REE composition, water masses and carbonate diagenesis. *Chem. Geol.* **280**, 180–190. Available at: http://dx.doi.org/10.1016/j.chemgeo.2010.11.007.

de Baar H. J. W., Bacon M. P., Brewer P. G. and Bruland K. W. (1985) Rare earth elements in the Pacific and Atlantic Oceans. *Geochim. Cosmochim. Acta* **49**, 1943–1959.

de Baar H. J. W., Bruland K. W., Schijf J., van Heuven S. M. A. C. and Behrens M. K. (2018) Low cerium among the dissolved rare earth elements in the central North Pacific Ocean. *Geochim. Cosmochim. Acta* **236**, 5–40. Available at: https://doi.org/10.1016/j.gca.2018.03.003.

Baturin G. N. (2000) Formation and Evolution of Phosphorite Grains and Nodules on the Namibian Shelf, from Recent to Pleistocene. In *Marine Authigenesis: From Global to Microbial* (eds. C. R. Glenn, L. Prévôt-Lucas, and J. Lucas). SEPM Society for Sedimentary Geology. Available at: https://doi.org/10.2110/pec.00.66.0185.

Baturin G. N. and Dubinchuk V. T. (2005) Authigenic minerals of uranium and rare earth elements in oceanic phosphorites. *Oceanology* **45**, 857–866.

Bau M. (1996) Controls on the fractionation of isovalent trace elements in magmatic and aqueous systems: evidence from Y/Ho, Zr/Hf, and lanthanide tetrad effect. *Contrib. to Mineral. Petrol.* **123**, 323–333. Available at:

http://link.springer.com/10.1007/s004100050159.

Bau M. and Alexander B. (2006) Preservation of primary REE patterns without Ce anomaly during dolomitization of Mid-Paleoproterozoic limestone and the potential re-establishment of marine anoxia immediately after the 'Great Oxidation Event'. *South African J. Geol.* **109**, 81–86.

Bau M., Balan S., Schmidt K. and Koschinsky A. (2010) Rare earth elements in mussel shells of the Mytilidae family as tracers for hidden and fossil high-temperature hydrothermal systems. *Earth Planet. Sci. Lett.* **299**, 310–316. Available at: http://dx.doi.org/10.1016/j.epsl.2010.09.011.

Bau M. and Dulski P. (1996) Distribution of yttrium and rare-earth elements in the Penge and Kuruman iron-formations, Transvaal Supergroup, South Africa. *Precambrian Res.* **79**, 37–55. Available at: http://linkinghub.elsevier.com/retrieve/pii/0301926895000879.

Bau M. and Dulski P. (1994) Evolution of the Yttrium-Holmium Systematics of Seawater Through Time. *Mineral. Mag.* **58A**, 61–62. Available at: http://www.minersoc.org/pages/Archive-MM/Volume_58A/58A-1-61.pdf.

Bau M. and Koschinsky A. (2009) Oxidative scavenging of cerium on hydrous Fe oxide: Evidence from the distribution of rare earth elements and yttrium between Fe oxides and Mn oxides in hydrogenetic ferromanganese crusts. *Geochem. J.* **43**, 37–47.

Bau M., Möller P. and Dulski P. (1997) Yttrium and lanthanides in eastern Mediterranean seawater and their fractionation during redox-cycling. *Mar. Chem.* **56**, 123–131.

Bright C. A., Cruse A. M., Lyons T. W., MacLeod K. G., Glascock M. D. and Ethington R. L. (2009) Seawater rare-earth element patterns preserved in apatite of Pennsylvanian conodonts? *Geochim. Cosmochim. Acta* **73**, 1609–1624. Available at: http://dx.doi.org/10.1016/j.gca.2008.12.014.

Brock J. and Schulz-Vogt H. N. (2011) Sulfide induces phosphate release from polyphosphate in cultures of a marine Beggiatoa strain. *ISME J.* **5**, 497–506.

Brüchert V., Currie B., Peard K. R., Lass U., Endler R., Dübecke A., Julies E., Leipe T. and Zitzmann S. (2006) Biogeochemical and physical control on shelf anoxia and water column

hydrogen sulphide in the Benguela coastal upwelling system off Namibia. In *Past and Present Water Column Anoxia* (ed. L. N. Neretin). Kluwer Academic Publishers, Dordrecht. pp. 161–193. Available at: http://link.springer.com/10.1007/1-4020-4297-3_07.

Byrne R. H., Liu X. and Schijf J. (1996) The influence of phosphate coprecipitation on rare earth distributions in natural waters. *Science (80-.).* **60**, 3341–3346.

Byrne R. H. and Sholkovitz E. R. (1996) Chapter 158 Marine chemistry and geochemistry of the lanthanides. *Handb. Phys. Chem. Rare Earths* **23**, 497–593. Available at: https://www.sciencedirect.com/science/article/pii/S0168127396230090 [Accessed October 16, 2018].

Chen J., Algeo T. J., Zhao L., Chen Z. Q., Cao L., Zhang L. and Li Y. (2015) Diagenetic uptake of rare earth elements by bioapatite, with an example from Lower Triassic conodonts of South China. *Earth-Science Rev.* **149**, 181–202. Available at: http://dx.doi.org/10.1016/j.earscirev.2015.01.013.

Coles S. K. P., Wright C. I., Sinclair D. A. and Van Den B. (2002) The potential for environmentally sound development of marine deposits of potassic and phosphatic minerals offshore, southern Africa. *Mar. Georesources Geotechnol.* **20**, 87–110.

Compton J. S. and Bergh E. W. (2016) Phosphorite deposits on the Namibian shelf. *Mar. Geol.* **380**, 290–314. Available at: http://dx.doi.org/10.1016/j.margeo.2016.04.006.

Compton J. S., Mulabisana J. and McMillan I. K. (2002) Origin and age of phosphorite from the Last Glacial Maximum to Holocene transgressive succession off the Orange ... Origin and age of phosphorite from the Last Glacial Maximum to Holocene transgressive succession o ¡ the Orange River , South Africa. *Mar. Geol.* **186**, 243–261.

Deng Y., Ren J., Guo Q., Cao J., Wang H. and Liu C. (2017) Rare earth element geochemistry characteristics of seawater and porewater from deep sea in western Pacific. *Sci. Rep.* **7**, 1–13. Available at: http://dx.doi.org/10.1038/s41598-017-16379-1.

Elderfield H. and Greaves M. J. (1982) The rare earth elements in seawater. *Nature* **296**, 214–219.

Elderfield H. and Sholkovitz E. R. (1987) Rare earth elements in the pore waters of reducing

nearshore sediments. *Earth Planet. Sci. Lett.* **82**, 280–288.

Elzinga E. J., Reeder R. J., Withers S. H., Peale R. E., Mason R. A., Beck K. M. and Hess W. P. (2002) EXAFS study of rare-earth element coordination in calcite. *Geochim. Cosmochim. Acta* **66**, 2875–2885.

Emeis K. C., Brüchert V., Currie B., Endler R., Ferdelman T., Kiessling A., Leipe T., Noli-Peard K., Struck U. and Vogt T. (2004) Shallow gas in shelf sediments of the Namibian coastal upwelling ecosystem. *Cont. Shelf Res.* **24**, 627–642.

Emsbo P., McLaughlin P. I., Breit G. N., du Bray E. A. and Koenig A. E. (2015) Rare earth elements in sedimentary phosphate deposits: Solution to the global REE crisis? *Gondwana Res.* **27**, 776–785. Available at: http://dx.doi.org/10.1016/j.gr.2014.10.008.

Fölmi K. B. (1996) The phosphorus cycle , phosphogenesis phosphate-rich deposits. **40**, 55–124.

Garcia-Solsona E., Jeandel C., Labatut M., Lacan F., Vance D., Chavagnac V. and Pradoux C. (2014) Rare earth elements and Nd isotopes tracing water mass mixing and particle-seawater interactions in the SE Atlantic. *Geochim. Cosmochim. Acta* **125**, 351–372. Available at: http://dx.doi.org/10.1016/j.gca.2013.10.009.

Glenn C. R., Föllmi K. B., Riggs S. R., Baturin G. N., Grimm K. A., Trappe J., Abed A. M., Galli-Olivier C., Garrison R. E., Ilyin a. V., Jehl C., Rohrlich V., Sadaqah R. M. Y., Schidlowski M., Sheldon R. E. and Seigmund H. (1994) Phosphorus and phosphorites: sedimentology and environments of formation. *Eclogae Geol. Helv.* **87**, 747–788. Available at: http://www.researchgate.net/publication/259590468_Phosphorus_and_Phosphorites_Sedimentology_and_Environments_of_Formation/file/72e7e52cd1642c7bac.pdf.

Goldhammer T., Brüchert V., Ferdelman T. G. and Zabel M. (2010) Microbial sequestration of phosphorus in anoxic upwelling sediments. *Nat. Geosci.* **3**, 557–561. Available at: http://dx.doi.org/10.1038/ngeo913.

Goldhammer T., Brunner B., Bernasconi S. M., Ferdelman T. G. and Zabel M. (2011) Phosphate oxygen isotopes: Insights into sedimentary phosphorus cycling from the Benguela upwelling system. *Geochim. Cosmochim. Acta* **75**, 3741–3756. Available at:

http://dx.doi.org/10.1016/j.gca.2011.04.006.

Haley B. A., Klinkhammer G. P. and McManus J. (2004) Rare earth elements in pore waters of marine sediments. *Geochim. Cosmochim. Acta* **68**, 1265–1279.

Herwartz D., Tütken T., Jochum K. P. and Sander P. M. (2013) Rare earth element systematics of fossil bone revealed by LA-ICPMS analysis. *Geochim. Cosmochim. Acta* **103**, 161–183.

Hood A. v. S., Planavsky N. J., Wallace M. W. and Wang X. (2018) The effects of diagenesis on geochemical paleoredox proxies in sedimentary carbonates. *Geochim. Cosmochim. Acta* **232**, 265–287. Available at: https://doi.org/10.1016/j.gca.2018.04.022.

Inthorn M., Mohrholz V. and Zabel M. (2006) Nepheloid layer distribution in the Benguela upwelling area offshore Namibia. *Deep. Res. Part I Oceanogr. Res. Pap.* **53**, 1423–1438.

Jahnke R. A. (1984) The synthesis and solubility of carbonate fluorapatite. *Am. J. Sci.* **284**, 58–78. Available at: http://www.ajsonline.org/cgi/doi/10.2475/ajs.284.1.58.

Jarvis I., Burnett W., Nathan Y., Almbaydin F., Attia A. K. M., Castro L., Flicoteaux R., Hilmy M. and Yn sain V. Q. A. S. A. Z. (1994) Phosphorite geochemistry state-of-the-art and environmental concerns.

Jochum K. P., Wilson S. A., Abouchami W., Amini M., Chmeleff J., Eisenhauer A., Hegner E., Iaccheri L. M., Kieffer B., Krause J., Mcdonough W. F., Mertz-Kraus R., Raczek I., Rudnick R. L., Scholz D., Steinhoefel G., Stoll B., Stracke A., Tonarini S., Weis D., Weis U. and Woodhead J. D. (2011) GSD-1G and MPI-DING Reference Glasses for In Situ and Bulk Isotopic Determination. *Geostand. Geoanalytical Res.* **35**, 193–226.

Joosu L., Lepland A., Kirsimäe K., Romashkin A. E., Roberts N. M. W., Martin A. P. and Črne A. E. (2015) The REE-composition and petrography of apatite in 2Ga Zaonega Formation, Russia: The environmental setting for phosphogenesis. *Chem. Geol.* **395**, 88–107.

Kim J.-H., Torres M. E., Haley B. A., Kastner M., Pohlman J. W., Riedel M. and Lee Y.-J. (2012) The effect of diagenesis and fluid migration on rare earth element distribution in pore fluids of the northern Cascadia accretionary margin. *Chem. Geol.* **291**, 152–165. Available at: http://dx.doi.org/10.1016/j.chemgeo.2011.10.010.

Knudsen A. C. and Gunter M. E. (2002) Sedimentary Phosphorites--An Example: Phosphoria Formation, Southeastern Idaho, U.S.A. *Rev. Mineral. Geochemistry* **48**, 363–389. Available at: http://rimg.geoscienceworld.org/cgi/doi/10.2138/rmg.2002.48.9.

Kocsis L., Gheerbrant E., Mouflih M., Cappetta H., Ulianov A., Chiaradia M. and Bardet N. (2016) Gradual changes in upwelled seawater conditions (redox, pH) from the late Cretaceous through early Paleogene at the northwest coast of Africa: Negative Ce anomaly trend recorded in fossil bio-apatite. *Chem. Geol.* **421**, 44–54.

Lécuyer C., Reynard B. and Grandjean P. (2004) Rare earth element evolution of Phanerozoic seawater recorded in biogenic apatites. *Chem. Geol.* **204**, 63–102.

Li F., Webb G. E., Algeo T. J., Kershaw S., Lu C., Oehlert A. M., Gong Q., Pourmand A. and Tan X. (2019) Modern carbonate ooids preserve ambient aqueous REE signatures. *Chem. Geol.* **509**, 163–177. Available at: https://doi.org/10.1016/j.chemgeo.2019.01.015.

Mänd K., Kirsimäe K., Lepland A., Crosby C. H., Bailey J. V., Konhauser K. O., Wirth R., Schreiber A. and Lumiste K. (2018) Authigenesis of biomorphic apatite particles from Benguela upwelling zone sediments off Namibia: The role of organic matter in sedimentary apatite nucleation and growth. *Geobiology*, 1–19. Available at: http://doi.wiley.com/10.1111/gbi.12309.

McArthur J. M. and Walsh J. N. (1984) Rare-earth geochemistry of phosphorites. *Chem. Geol.* **47**, 191–220.

Minami M., Masuda A., Takahashi K., Adachi M. and Shimizu H. (1998) Y-Ho fractionation and lanthanide tetrad effect observed in cherts. *Geochem. J.* **32**, 405–419.

Moffett J. W. (1990) Microbially mediated cerium oxidation in sea water. *Nature* **345**, 421. Available at: https://doi.org/10.1038/345421a0.

Morad S. and Felitsyn S. (2001) Identification of primary Ce-anomaly signatures in fossil biogenic apatite: Implication for the Cambrian oceanic anoxia and phosphogenesis. *Sediment. Geol.* **143**, 259–264.

Murray J. S. and Renard A. F. (1891) Report on deep-sea deposits based on the specimens collected during the voyage of H.M.S. Challenger in the years 1872 to 1876. , 391–400.

Nozaki Y., Zhang J. and Amakawa H. (1997) The fractionation between Y and Ho in the marine environment. *Earth Planet. Sci. Lett.* **148**, 329–340.

Pattan J. N., Pearce N. J. G. and Mislankar P. G. (2005) Constraints in using Cerium-anomaly of bulk sediments as an indicator of paleo bottom water redox environment: A case study from the Central Indian Ocean Basin. *Chem. Geol.* **221**, 260–278.

Piper D. Z. and Bau M. (2013) Normalized Rare Earth Elements in Water, Sediments, and Wine: Identifying Sources and Environmental Redox Conditions. *Am. J. Anal. Chem.* **04**, 69–83. Available at: http://www.scirp.org/journal/doi.aspx?DOI=10.4236/ajac.2013.410A1009.

Pufahl P. K. and Grimm K. A. (2003) Coated phosphate grains: Proxy for physical, chemical, and ecological changes in seawater. *Geology* **31**, 801–804.

Reynard B., Lécuyer C. and Grandjean P. (1999) Crystal-chemical controls on rare-earth element concentrations in fossil biogenic apatites and implications for paleoenvironmental reconstructions. *Chem. Geol.* **155**, 233–241.

Rigali M. J., Brady P. V. and Moore R. C. (2016) Radionuclide removal by apatite. *Am. Mineral.* **101**, 2611–2619.

Ruttenberg K. C. and Berner R. A. (1993) Authigenic apatite formation and burial in sediments from non-upwelling, continental margin environments. *Geochim. Cosmochim. Acta* **57**, 991–1007. Available at: https://www.sciencedirect.com/science/article/pii/001670379390035U [Accessed March 15, 2019].

Schulz H., Brinkhoff T., Ferdelman T., Hernandez Marine M., Teske A. and Jorgensen B. B. (1999) Dense Populations of a Giant Sulfur Bacterium in Namibian Shelf Sediments. *Science (80-.).* **284**, 493–495. Available at: http://www.sciencemag.org/cgi/doi/10.1126/science.284.5413.493.

Schulz H. and Schulz H. N. (2005) Large Sulfur Bacteria and the Formation of Phosphorite. *Science (80-.).* **307**, 416–418. Available at: http://www.sciencemag.org/cgi/doi/10.1126/science.1103096.

Shields G. and Stille P. (2001) Diagenetic constraints on the use of cerium anomalies as

palaeoseawater redox proxies: An isotopic and REE study of Cambrian phosphorites. *Chem. Geol.* **175**, 29–48.

Shields G. and Webb G. E. (2004) Has the REE composition of seawater changed over geological time? *Chem. Geol.* **204**, 103–107.

Sholkovitz E. R., Piepgras D. J. and Jacobsen S. B. (1989) The pore water chemistry of rare earth elements in Buzzards Bay sediments. *Geochim. Cosmochim. Acta* **53**, 2847–2856.

Skinner L. C., Sadekov A., Brandon M., M.Greaves, Plancherel Y., de la Fuente M., Gottschalk J., Souanef-Ureta S., Sevilgen D. S. and Scrivner A. E. (2018) Rare Earth Elements in early-diagenetic foraminifer 'coatings': pore-water controls and potential palaeoceanographic applications. *Geochim. Cosmochim. Acta*. Available at: https://linkinghub.elsevier.com/retrieve/pii/S0016703718306136.

Takahashi Y., Hayasaka Y., Morita K., Kashiwabara T., Nakada R., Marcus M. A., Kato K., Tanaka K. and Shimizu H. (2015) Transfer of rare earth elements (REE) from manganese oxides to phosphates during early diagenesis in pelagic sediments inferred from REE patterns, X-ray absorption spectroscopy, and chemical leaching method. *Geochem. J.* **49**, 653–674.

Taylor S. R. and McLennan S. M. (1985) The Continental Crust: Its Composition and Evolution. An Examination of the Geochemical Record Preserved in Sedimentary Rocks. *Cont. Crust Its Compos. Evol. An Exam. Geochemical Rec. Preserv. Sediment. Rocks.*, 312.

Tostevin R., Shields G. A., Tarbuck G. M., He T., Clarkson M. O. and Wood R. A. (2016) Effective use of cerium anomalies as a redox proxy in carbonate-dominated marine settings. *Chem. Geol.* **438**, 146–162. Available at: http://dx.doi.org/10.1016/j.chemgeo.2016.06.027.

Tribovillard N., Algeo T. J., Lyons T. and Riboulleau A. (2006) Trace metals as paleoredox and paleoproductivity proxies: An update. *Chem. Geol.* **232**, 12–32.

Trotter J. A., Barnes C. R. and McCracken A. D. (2016) Rare earth elements in conodont apatite: Seawater or pore-water signatures? *Palaeogeogr. Palaeoclimatol. Palaeoecol.* **462**, 92–100. Available at: http://dx.doi.org/10.1016/j.palaeo.2016.09.007.

Trueman C. N. (2013) Chemical taphonomy of biomineralized tissues. *Palaeontology* **56**, 475–

486.

Voigt M., Voigt M., Mavromatis V. and Oelkers E. H. (2017) The experimental determination of REE partition coefficients in the water- calcite system The experimental determination of REE partition coe ffi cients in the water- calcite system. *Chem. Geol.* **462**, 30–43. Available at: http://dx.doi.org/10.1016/j.chemgeo.2017.04.024.

Wallace M. W., Hood A. vS., Shuster A., Greig A., Planavsky N. J. and Reed C. P. (2017) Oxygenation history of the Neoproterozoic to early Phanerozoic and the rise of land plants. *Earth Planet. Sci. Lett.* **466**, 12–19. Available at: http://dx.doi.org/10.1016/j.epsl.2017.02.046.

Wang Z. L. and Yamada M. (2007) Geochemistry of dissolved rare earth elements in the Equatorial Pacific Ocean. *Environ. Geol.* **52**, 779–787.

Watkins R. T., Nathan Y. and Bremner J. M. (1995) Rare earth elements in phosphorite and associated sediment from the Namibian and South African continental shelves. *Mar. Geol.* **129**, 111–128.

Webb G. E. ., Nothdurft L. D., Kamber B. S., Kloprogge J. T. and Zhao J.-X. (2009) Rare earth element geochemistry of scleractinian coral skeleton during meteoric diagenesis: a sequence through neomorphism of aragonite to calcite. *Sedimentology* **56**, 1433–1463. Available at: http://doi.wiley.com/10.1111/j.1365-3091.2008.01041.x.

Zhang J. and Nozaki Y. (1996) Rare earth elements and yttrium in seawater: ICP-MS determinations in the East Caroline, Coral Sea, and South Fiji basins of the western South Pacific Ocean. *Geochim. Cosmochim. Acta* **60**, 4631–4644.

Zhao L., Chen Z. Q., Algeo T. J., Chen J., Chen Y., Tong J., Gao S., Zhou L., Hu Z. and Liu Y. (2013) Rare-earth element patterns in conodont albid crowns: Evidence for massive inputs of volcanic ash during the latest Permian biocrisis? *Glob. Planet. Change* **105**, 135–151. Available at: http://dx.doi.org/10.1016/j.gloplacha.2012.09.001.

Zhu B., Jiang S. Y., Yang J. H., Pi D., Ling H. F. and Chen Y. Q. (2014) Rare earth element and SrNd isotope geochemistry of phosphate nodules from the lower Cambrian Niutitang Formation, NW Hunan Province, South China. *Palaeogeogr. Palaeoclimatol. Palaeoecol.*

398, 132–143. Available at: http://dx.doi.org/10.1016/j.palaeo.2013.10.002.

Zoss R., Medina Ferrer F., Flood B. E., Jones D. S., Louw D. C. and Bailey J. (2018) Microbial communities associated with phosphogenic sediments and phosphoclast-associated DNA of the Benguela upwelling system. *Geobiology* **17**, 76–90.

Figure captions

Figure 1. Simplified geological map of the Namibian shelf with the locations of coring sites used in this study. Modified after Baturin (2000) and Mänd et al. (2018).

Figure 2. Backscattered scanning electron microscope images of the apatite grains: (a-b) irregular authigenic, concretionary apatitic grains from core 25005 with low S-content, (c,d,f) reworked and rounded pelletal apatitic grains from core CG4 (e) showing concentric layering in some cases.

Figure 3. Elemental maps of a concretionary apatitic grain from core 25005, depth 2-3 cm.

Figure 4. Elemental maps of a pelletal apatitic grain from core CG4, depth 10-11 cm. Areas with low Ca and P are high in either Si, Fe+S or Ba+S.

Figure 5. Apatite ∑REE+Y concentrations from cores 25005 and CG4: (a) enrichment zone of pelletal apatitic grains from core CG4, (b) enrichment zone of concretionary apatitic grains from core 25005, (c) central part of pelletal apatitic grains from core CG4, (d) central part of concretionary apatitic grains from core 25005.

Figure 6. Backscattered scanning electron microscope images of concretionary apatitic grains from core 25005 and LA-ICP-MS elemental distribution maps showing a clear enrichment of REE+Y in the outer rim of the grains. Scale bars are in mg/kg and show different values for each individual element.

Figure 7. Backscattered scanning electron microscope images of pelletal apatitic grains from core CG4 and LA-ICP-MS elemental distribution with enrichment of REE+Y in the outer rim of the grains. Scale bars are in mg/kg and show different values for each individual element. The grain on the right shows concentric layering and several zones of apatite growth. The surface of

the internal zone shows enrichment in REE+Y, U and Th similar to the enrichment zone of the external layers of the whole grain.

Figure 8. LA-ICP-MS line scans across the grain centers showing the distribution of REE+Y in different types of apatitic grains (five-point average). Note that the degree of enrichment is significantly higher at the surface layers of the pelletal grains (CG4).

Figure 9. Representative PAAS normalized REE+Y patterns of apatite from: a) core CG4, grain center, b) core 25005, grain center, c) core CG4, enrichment zone, d) 25005, enrichment zone.

Figure 10. Ce/Ce* vs Pr/Pr* plot. Field I: no La or Ce anomaly; Field IIa: apparent negative Ce anomaly, due to positive La anomaly, field IIb: apparent positive Ce anomaly, due to negative La anomaly; Field IIIa: true positive Ce anomaly; Field IIIb: true negative Ce anomaly. Modified after Bau and Dulski (1996).

Figure 11. Y/Ho vs SmN/YbN plot showing a clear decrease in Y/Ho ratios and a growth of SmN/YbN values with increasing diagenesis. Modified after Kocsis et al. (2016).

Figure 12. REE normalized plots: a) LaN/SmN vs LaN/YbN showing increasing LREE concentrations during post-depositional porewater-rock interaction and b) LaN/NdN vs Y/Y* showing increasing diagentic alteration with lowering Y/Y* and LaN/NdN values. Modified after Reynard et al. (1997) and Auer et al. (2017).

Figure 13. Conceptual model of changes in apatitic grain REE+Y composition during diagenesis. (a) During initial precipitation the REE+Y are incorporated from oxic sea water or very shallow pore-water; (b) under suboxic-sulfidic conditions the REE+Y are incorporated to the exterior layers of the grain from suboxic-sulfidic pore-water while still displaying some seawater-like features (HREE enrichment and high Y/Ho ratios); (c) after longer periods of exposure to suboxic-sulfidic pore-water, the enrichment zone develops a shale like pattern with a positive Ce anomaly, while the interior acquires a higher LREE/HREE ratio and lower Y/Ho values.

Supplementary table captions

Supplementary table 1. LA-ICP-MS spot measurement data from apatite grain centers.

Supplementary table 2. LA-ICP-MS spot measurement data from apatite grain exteriors.

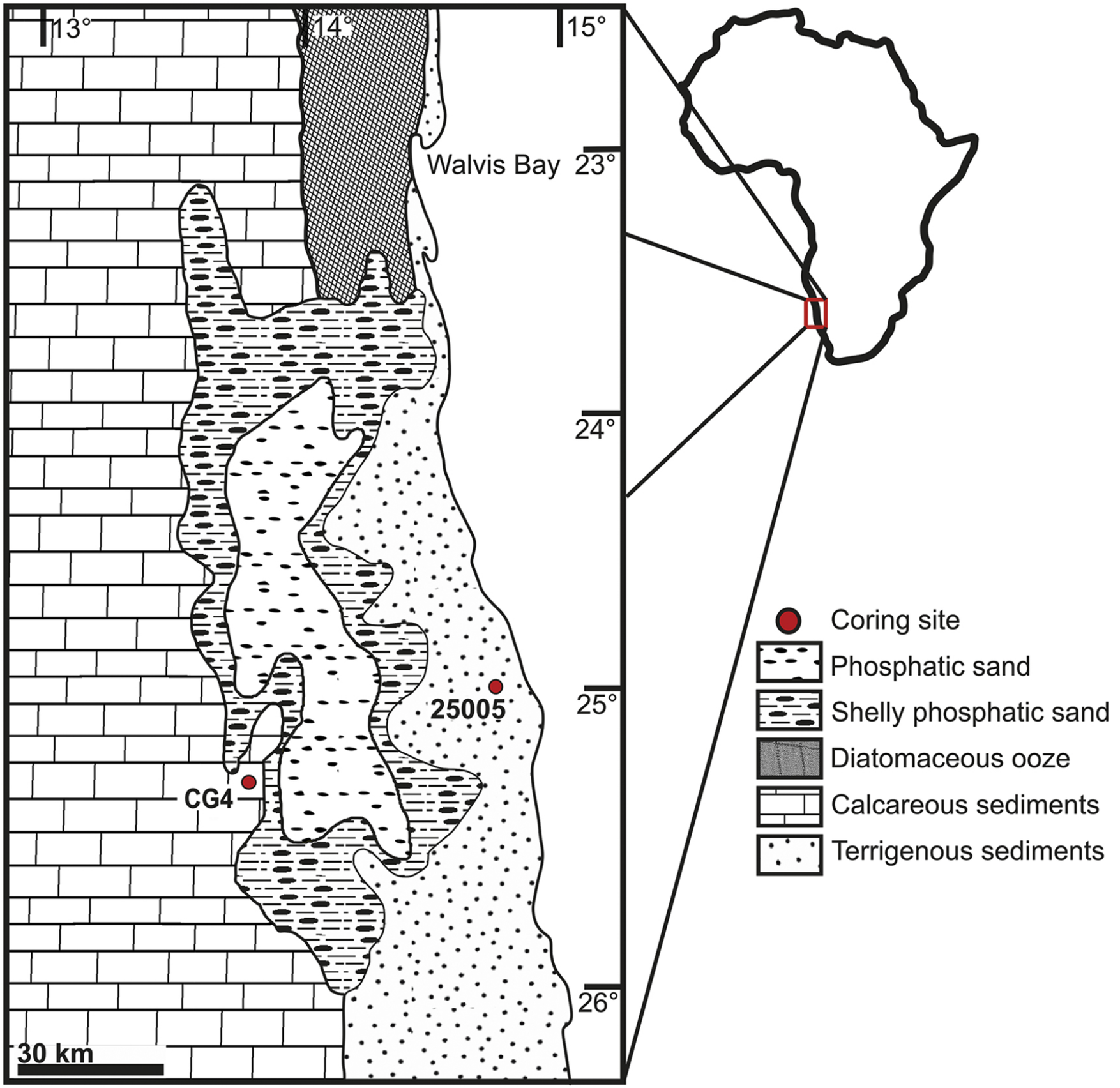
13°
14°
15°
Walvis Bay
23°
24°
25°
26°
25005
CG4
30 km
Coring site
Phosphatic sand
Shelly phosphatic sand
Diatomaceous ooze
Calcareous sediments
Terrigenous sediments

Figure 1

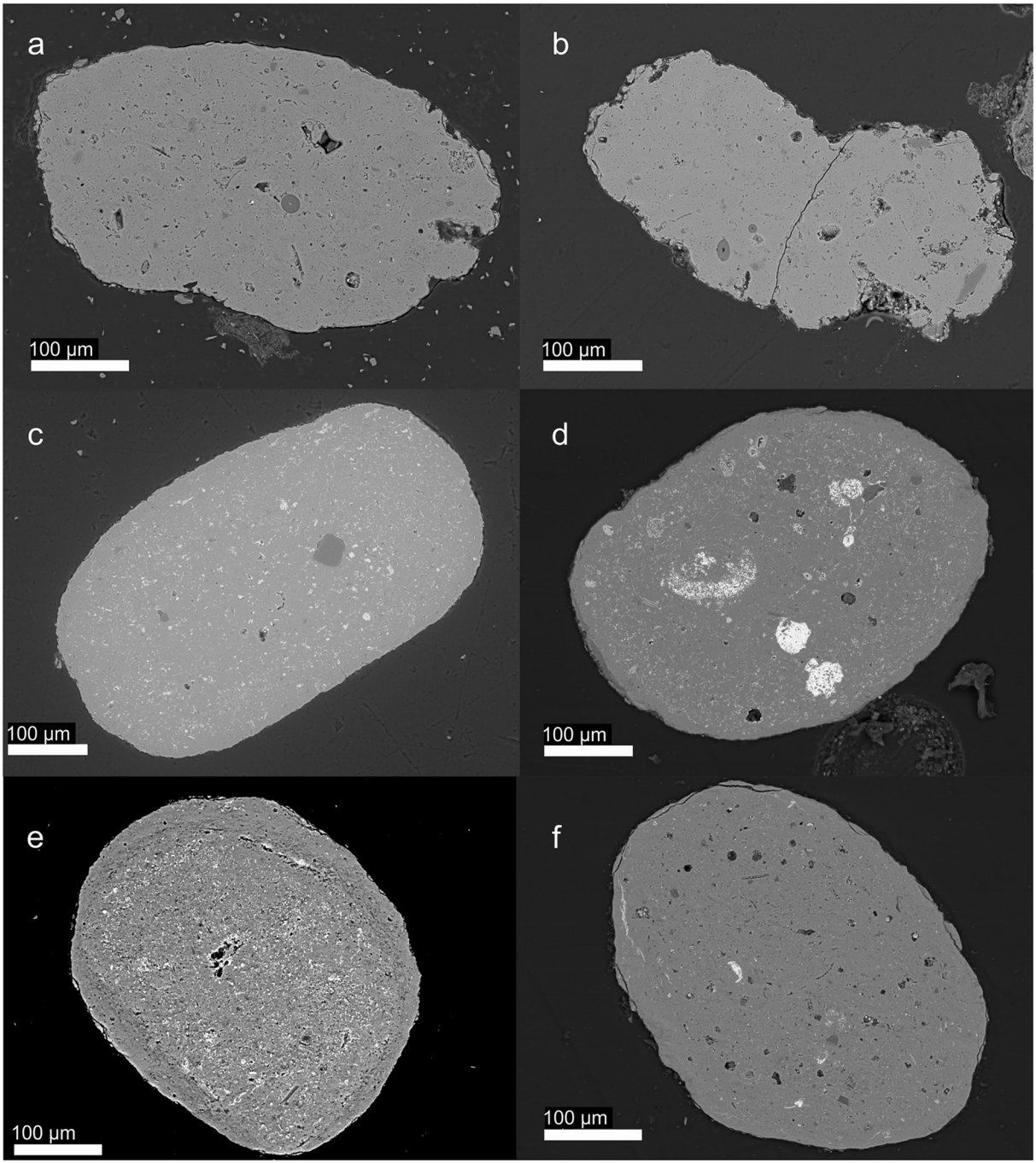

Figure 2

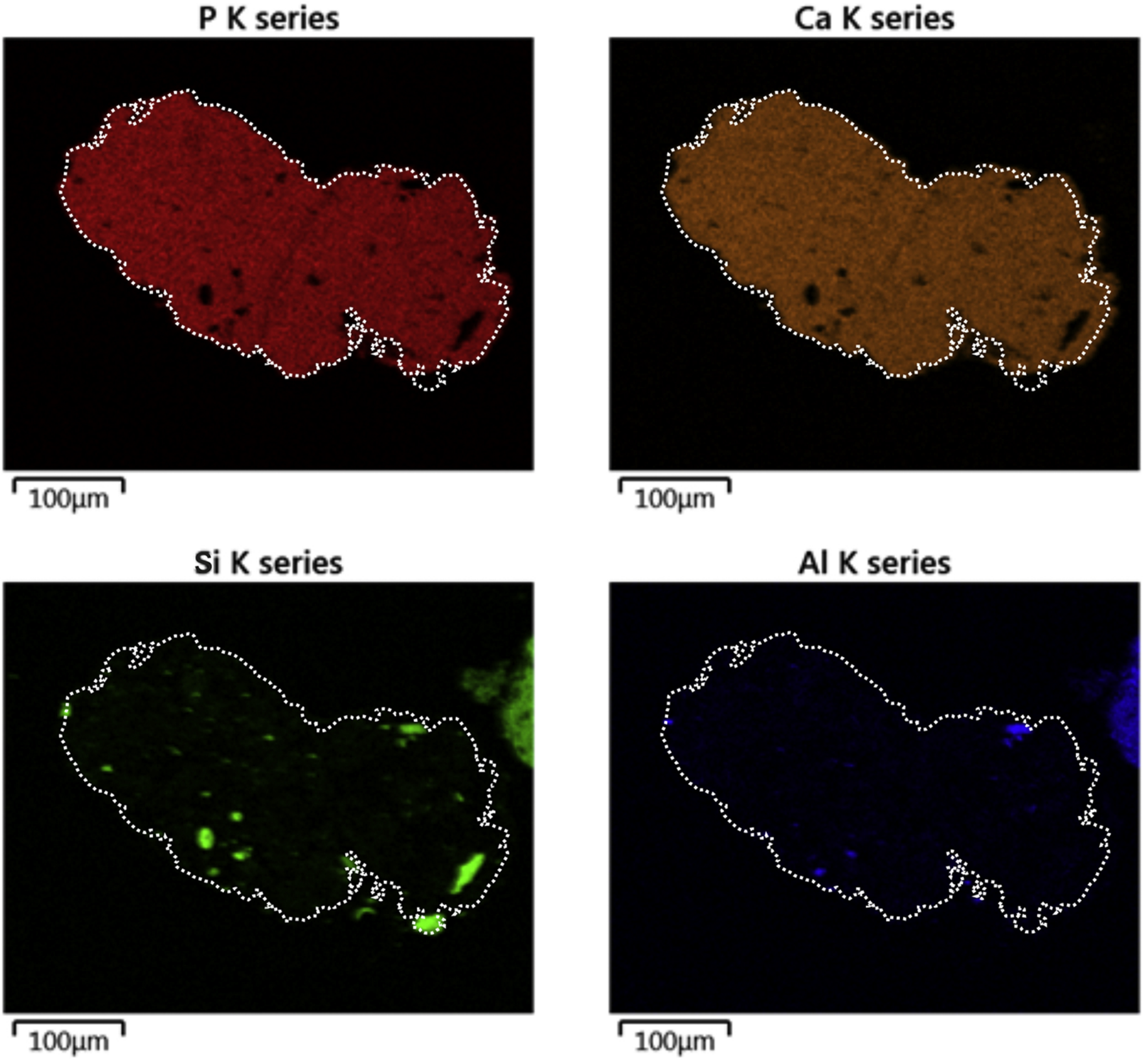
P K series
100µm
Ca K series
100µm
Si K series
100µm
Al K series
100µm

Figure 3

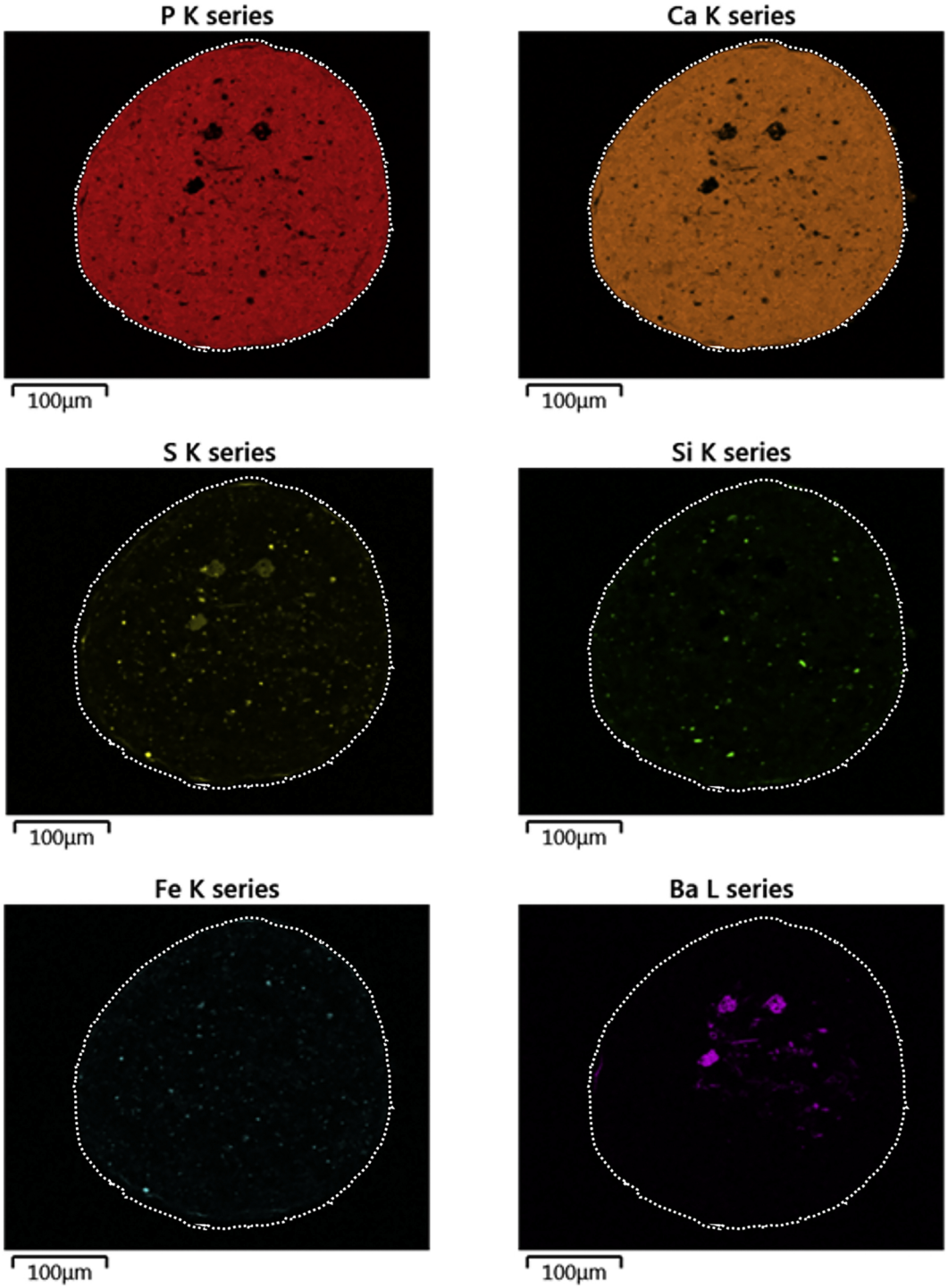
P K series
100µm
Ca K series
100µm
S K series
100µm
Si K series
100µm
Fe K series
100µm
Ba L series
100µm

Figure 4

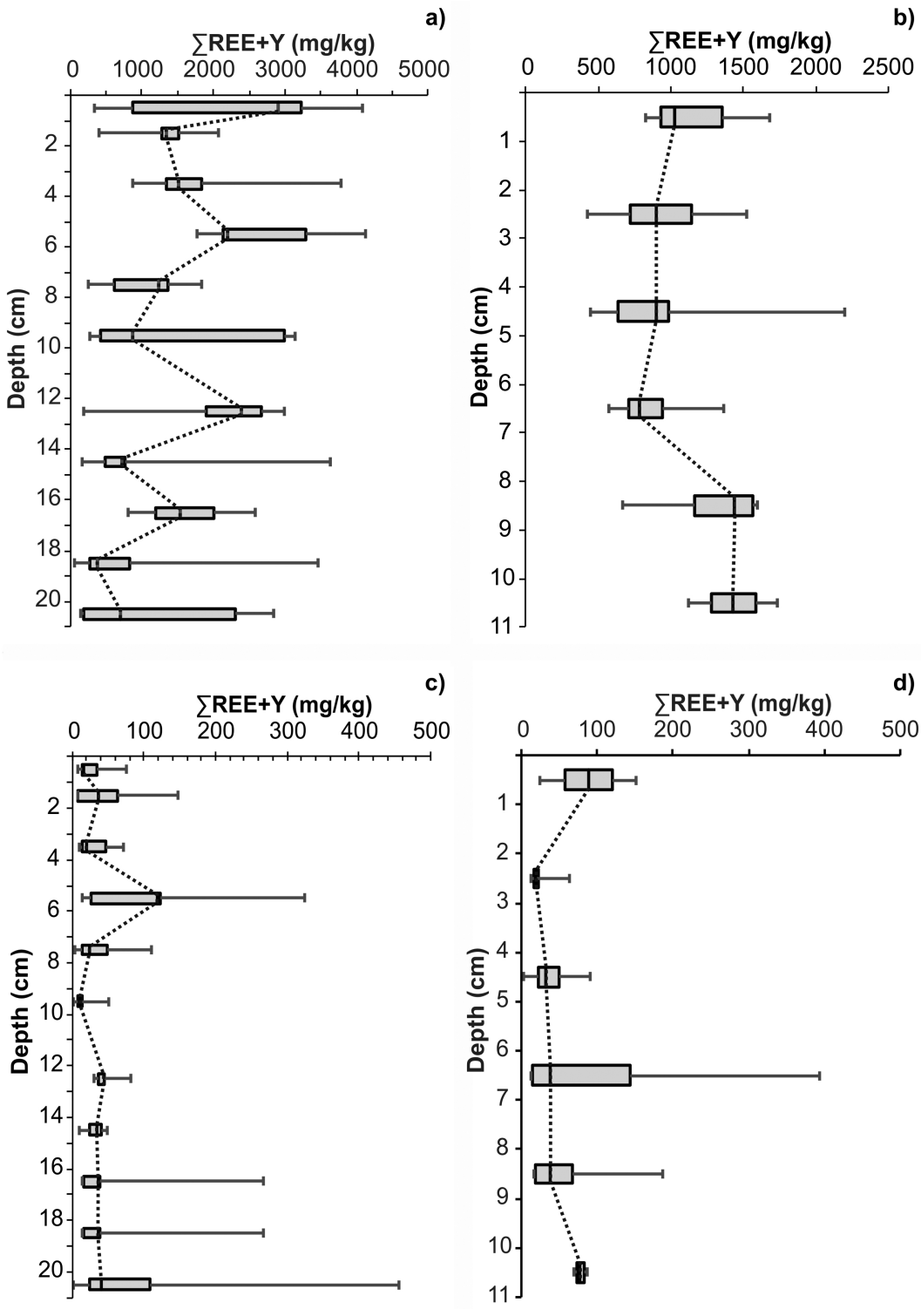
a)
∑REE+Y (mg/kg)
0 1000 2000 3000 4000 5000
Depth (cm)
2 4 6 8 10 12 14 16 18 20
b)
∑REE+Y (mg/kg)
0 500 1000 1500 2000 2500
Depth (cm)
1 2 3 4 5 6 7 8 9 10 11
c)
∑REE+Y (mg/kg)
0 100 200 300 400 500
Depth (cm)
2 4 6 8 10 12 14 16 18 20
d)
∑REE+Y (mg/kg)
0 100 200 300 400 500
Depth (cm)
1 2 3 4 5 6 7 8 9 10 11

Figure 5

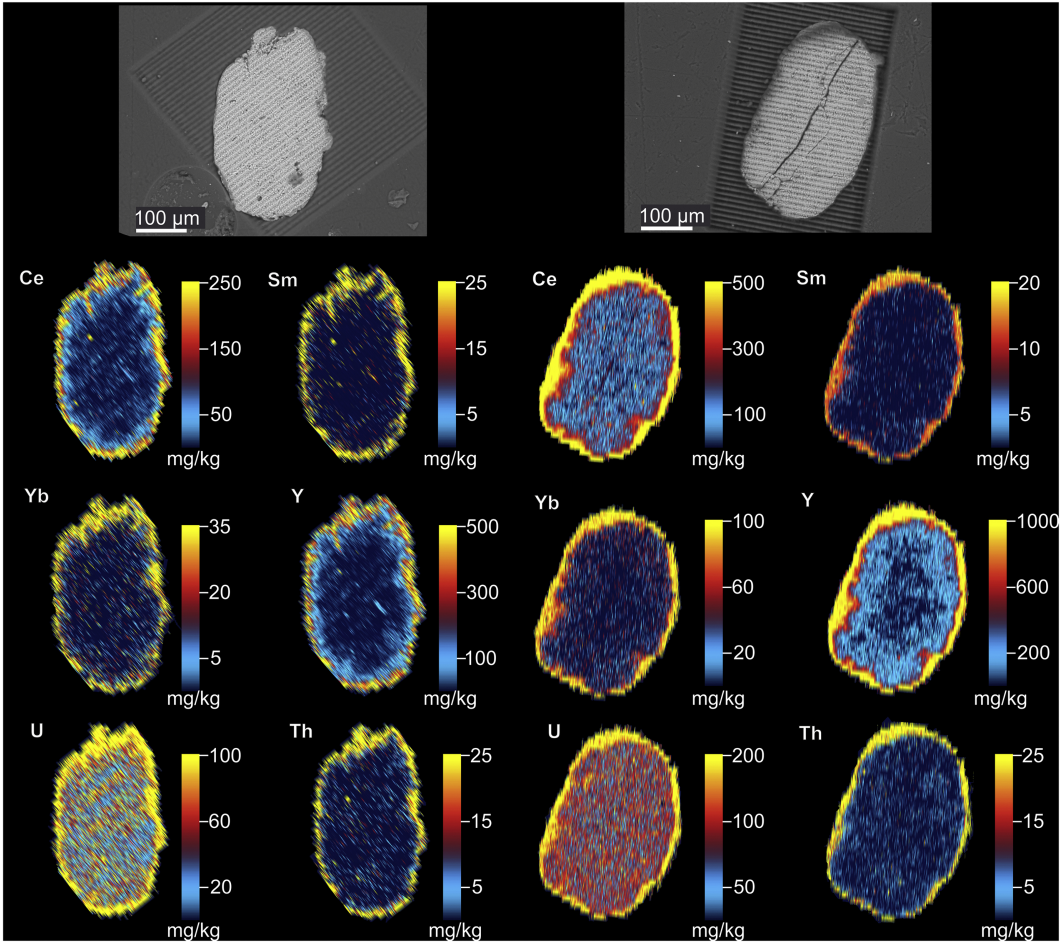
100 µm
100 µm
Ce
250
150
50
mg/kg
Sm
25
15
5
mg/kg
Ce
500
300
100
mg/kg
Sm
20
10
5
mg/kg
Yb
35
20
5
mg/kg
Y
500
300
100
mg/kg
Yb
100
60
20
mg/kg
Y
1000
600
200
mg/kg
U
100
60
20
mg/kg
Th
25
15
5
mg/kg
U
200
100
50
mg/kg
Th
25
15
5
mg/kg

Figure 6

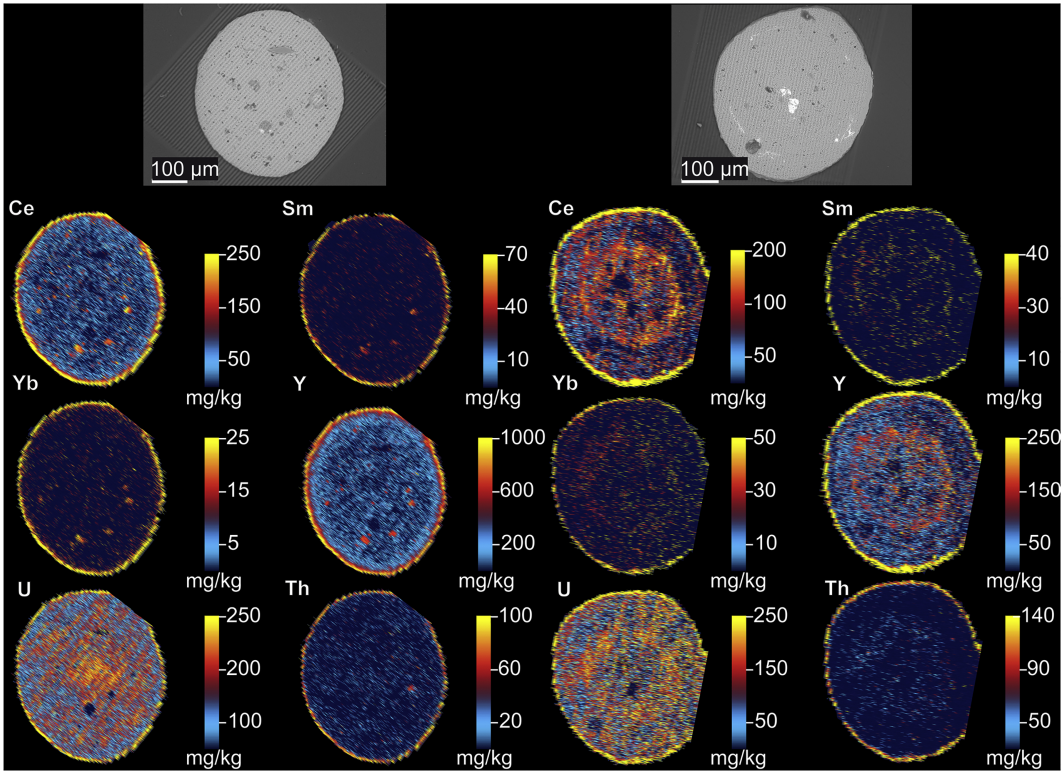
100 µm
100 µm
Ce
250
150
50
mg/kg
Sm
70
40
10
mg/kg
Yb
25
15
5
mg/kg
Y
1000
600
200
mg/kg
U
250
200
100
mg/kg
Th
100
60
20
mg/kg
Ce
200
100
50
mg/kg
Sm
40
30
10
mg/kg
Yb
50
30
10
mg/kg
Y
250
150
50
mg/kg
U
250
150
50
mg/kg
Th
140
90
50
mg/kg

Figure 7

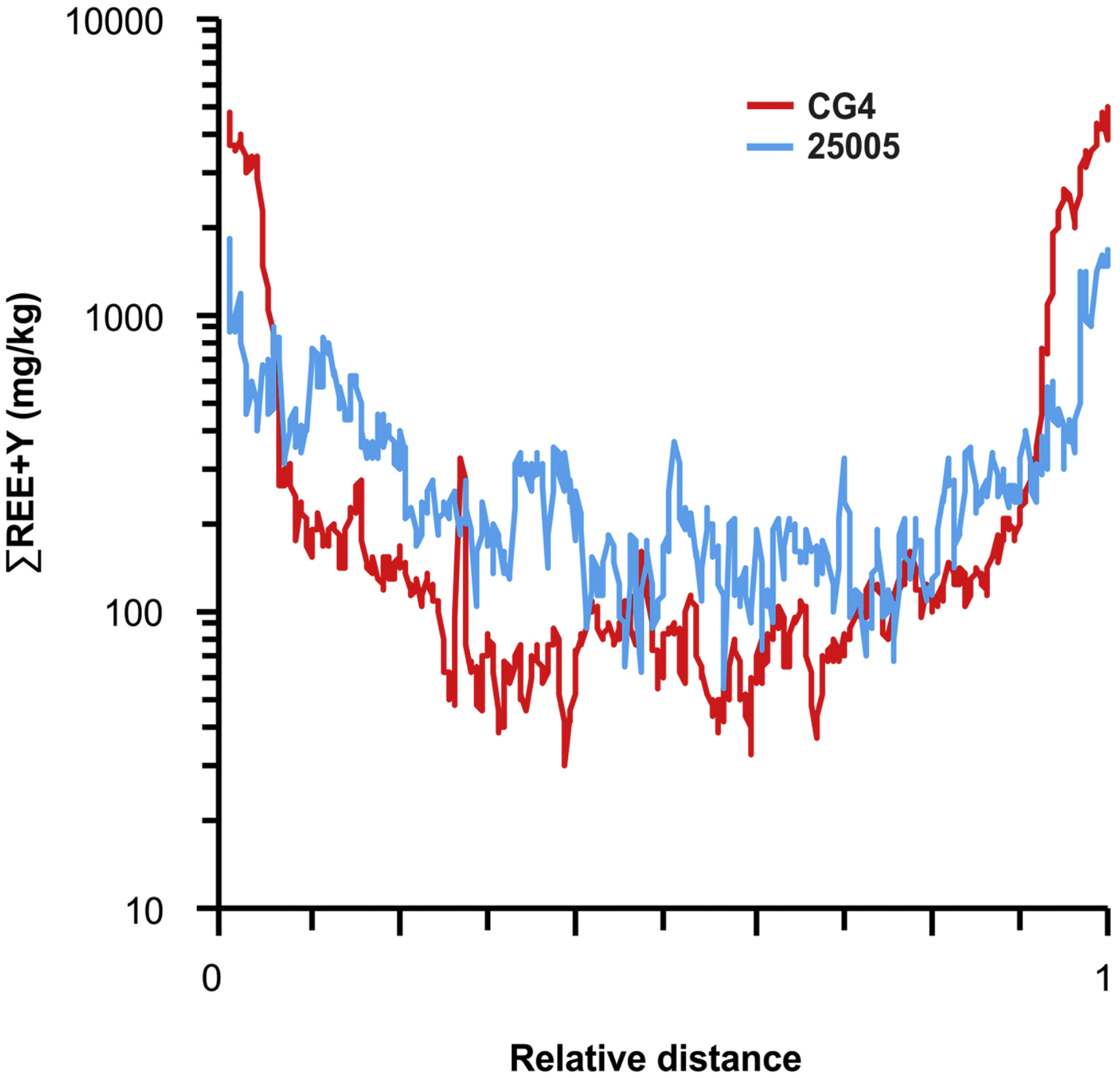

Figure 8

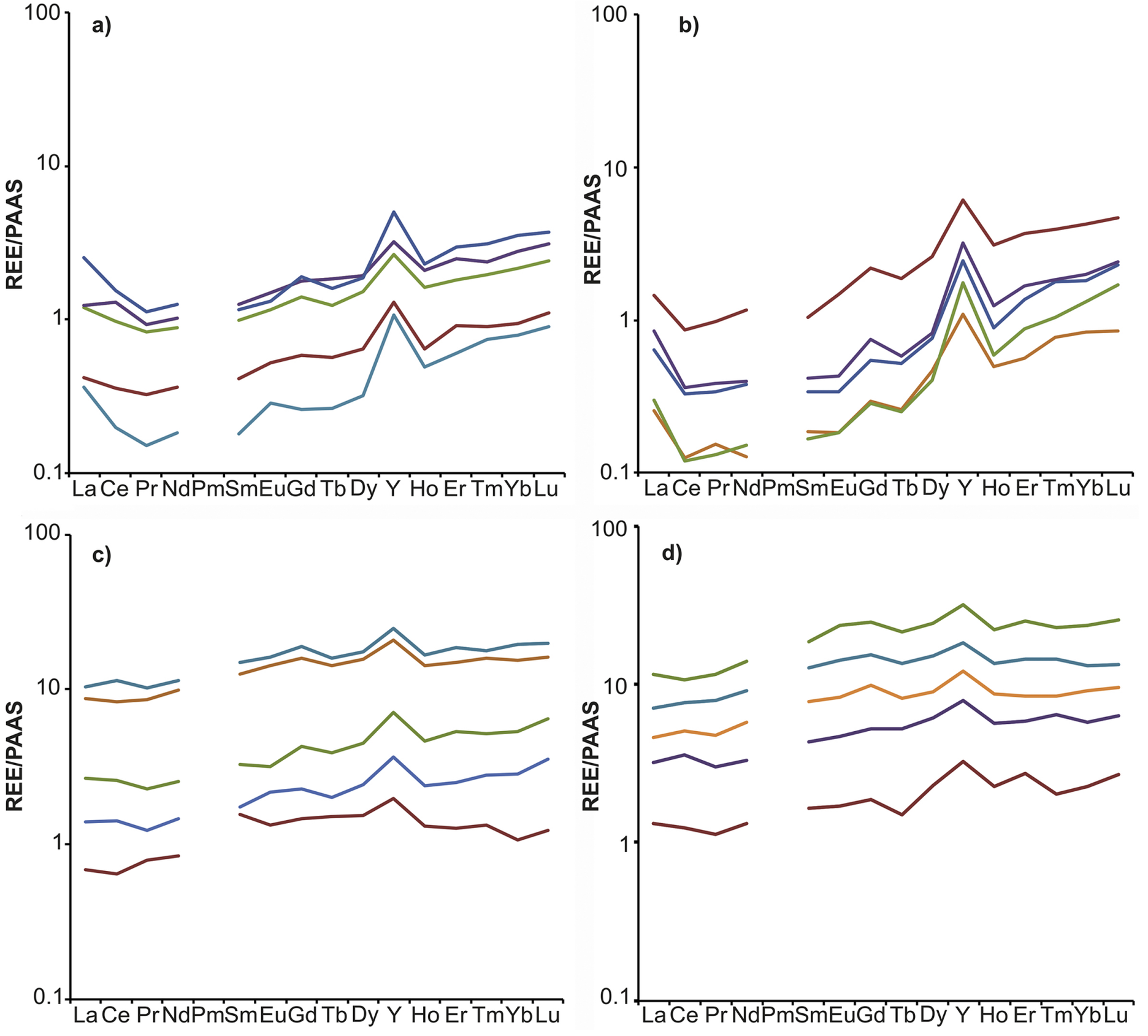
a)
b)
c)
d)
100
10
1
0.1
REE/PAAS
La Ce Pr Nd Pm Sm Eu Gd Tb Dy Y Ho Er Tm Yb Lu

Figure 9

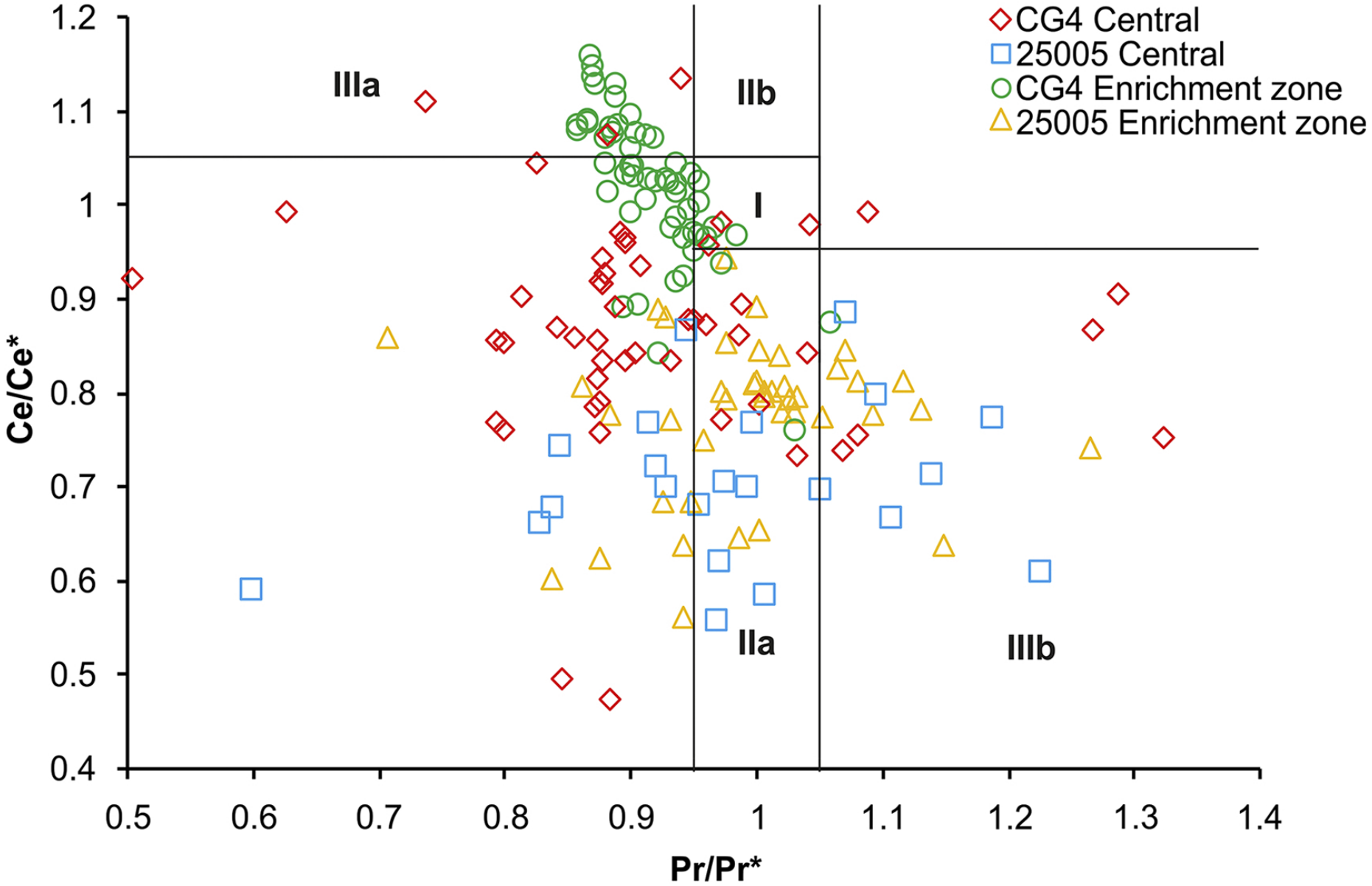
CG4 Central
25005 Central
CG4 Enrichment zone
25005 Enrichment zone
IIIa
IIb
I
IIa
IIIb
Ce/Ce*
Pr/Pr*
1.2
1.1
1
0.9
0.8
0.7
0.6
0.5
0.4
0.5
0.6
0.7
0.8
0.9
1
1.1
1.2
1.3
1.4

Figure 10

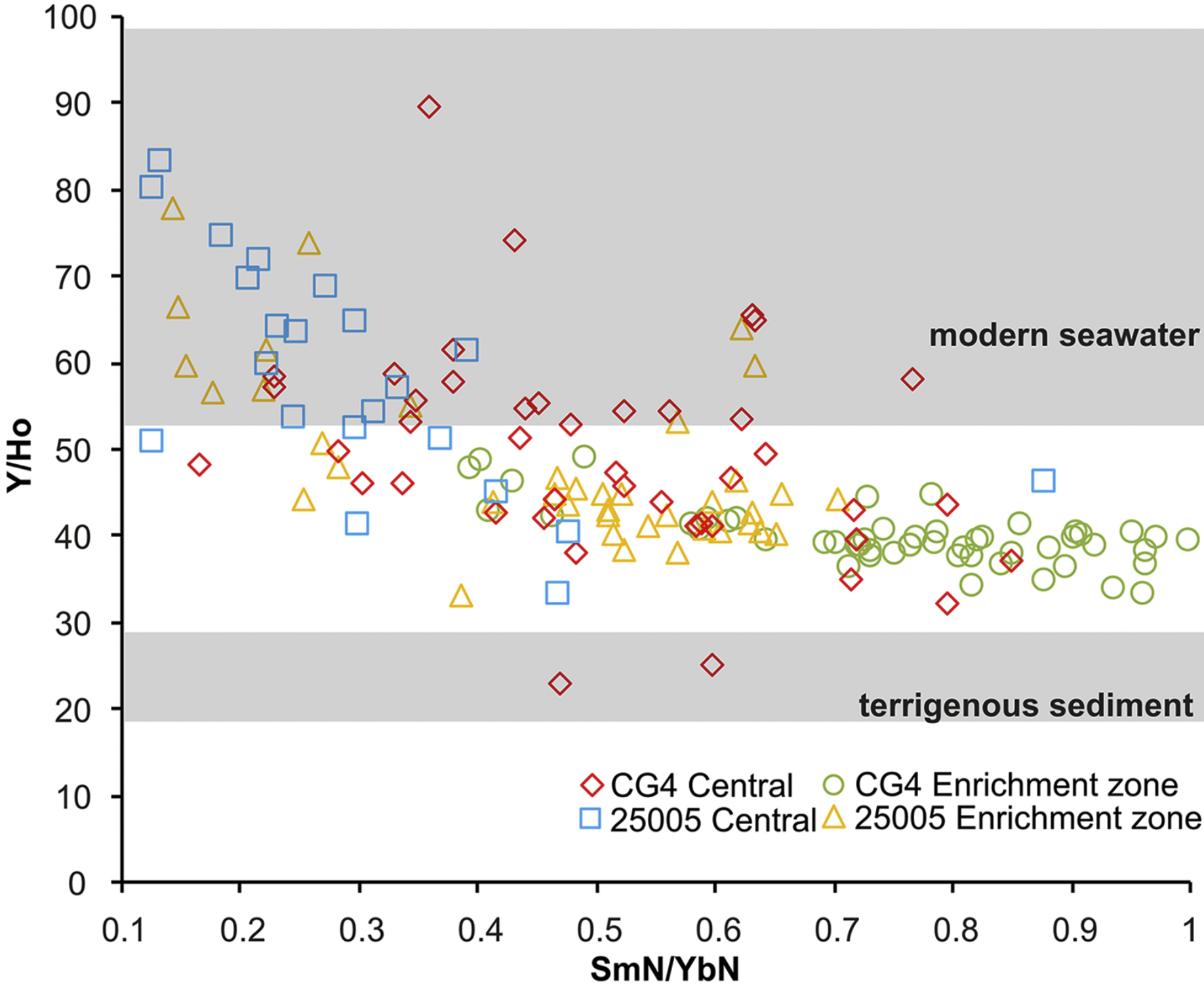
100
90
80
70
60
50
40
30
20
10
0
Y/Ho
0.1
0.2
0.3
0.4
0.5
0.6
0.7
0.8
0.9
1
SmN/YbN
modern seawater
terrigenous sediment
CG4 Central
CG4 Enrichment zone
25005 Central
25005 Enrichment zone

Figure 11

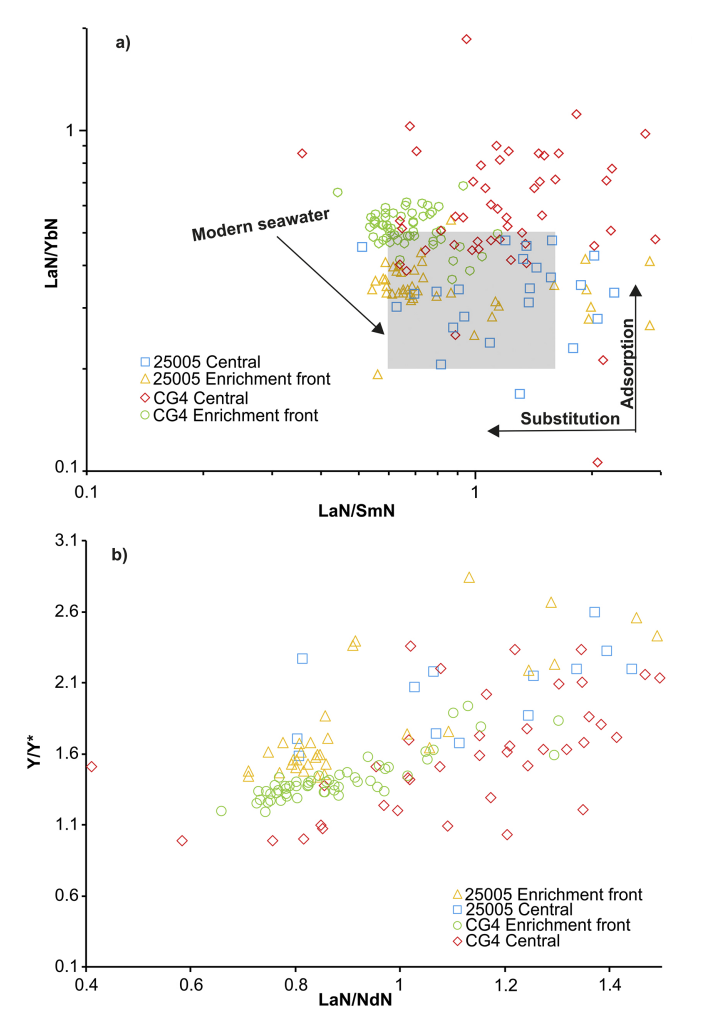
a)
LaN/YbN
1
0.1
0.1
1
LaN/SmN
Modern seawater
25005 Central
25005 Enrichment front
CG4 Central
CG4 Enrichment front
Substitution
Adsorption
b)
Y/Y*
3.1
2.6
2.1
1.6
1.1
0.6
0.1
0.4
0.6
0.8
1
1.2
1.4
LaN/NdN
25005 Enrichment front
25005 Central
CG4 Enrichment front
CG4 Central

Figure 12

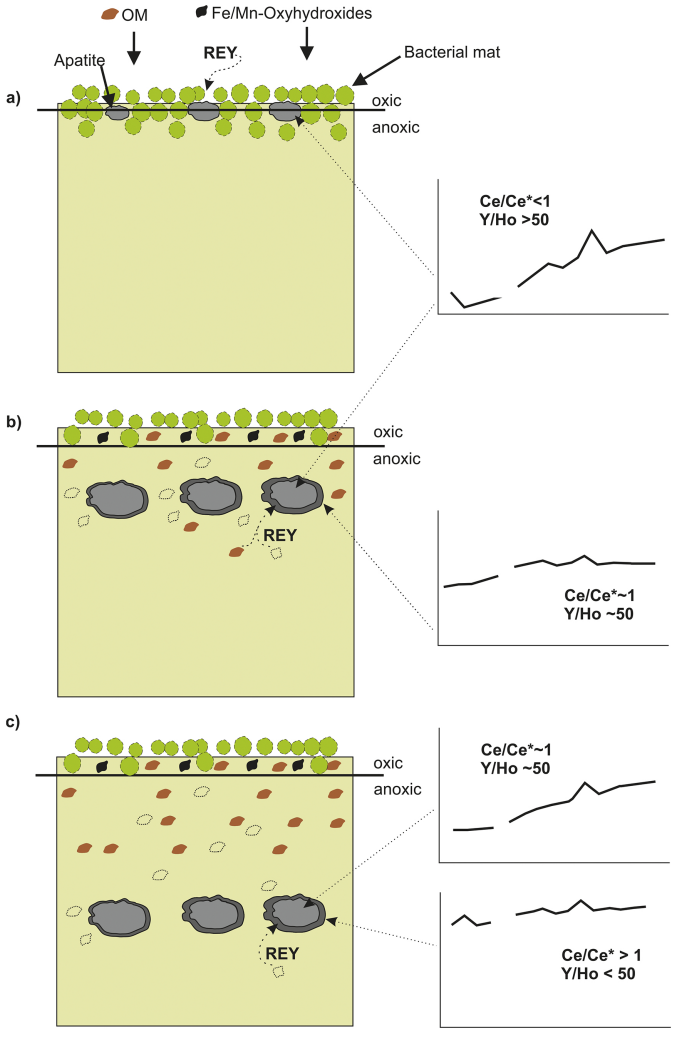
OM
Fe/Mn-Oxyhydroxides
Apatite
REY
Bacterial mat
a)
oxic
anoxic
Ce/Ce*<1
Y/Ho >50
b)
oxic
anoxic
REY
Ce/Ce*~1
Y/Ho ~50
c)
oxic
anoxic
Ce/Ce*~1
Y/Ho ~50
REY
Ce/Ce* > 1
Y/Ho < 50

Figure 13